

NATIONAL ADVISORY COMMITTEE FOR AERONAUTICS

RESEARCH MEMORANDUM

for the

Air Materiel Command, U. S. Air Force

STABILITY AND CONTROL CHARACTERISTICS AT LOW

SPEED OF A $\frac{1}{5}$ -SCALE MODEL OF THE EDO 142

HYDRO-SKI RESEARCH AIRPLANE

By John M. Riebe, Richard G. MacLeod,
and William C. Moseley, Jr.

SUMMARY

An investigation was made in the Langley 300 MPH 7- by 10-foot tunnel to determine the low-speed stability and control characteristics and the jet-engine duct-inlet pressure recovery characteristics of a $\frac{1}{5}$ -scale model of the Edo 142 hydro-ski research airplane.

Results of the model tests indicated elevator-fixed static longitudinal stability amounting generally to a static margin of about 0.19 mean aerodynamic chord throughout most of the lift-coefficient range. The model was very stable longitudinally near the stall and, consequently, the maximum trim lift coefficient available from the elevators (ruddervators) was limited to 1.09. A higher maximum trim lift coefficient (1.2) could be obtained by extending the leading-edge slats inboard 0.12 semispan from the original position. The model had approximately neutral static directional stability over the yaw angle range of $\pm 5^\circ$ at low angles of attack which could be improved by blunting the rearward end of the hull. The effective dihedral of the model was high throughout the lift-coefficient range mainly because of the large vee tail. The effectiveness of the rudder (ruddervators) was adequate to trim the model through the yaw range of $\pm 15^\circ$ at both low and high up-elevator (ruddervator) trim angles. The aileron effectiveness was satisfactory up to and beyond the angle of attack for maximum lift coefficient.

Of several configurations of the jet-engine duct inlet, which was located on top of the fuselage, a duct with a trumpet-shaped ramp with

~~CONFIDENTIAL~~

medium-height walls appeared to give the most uniform flow distribution and the highest ram recovery at the location of the engine compressor.

INTRODUCTION

An investigation of the stability and control characteristics at low speed of a $\frac{1}{5}$ -scale model of the Edo 142 hydro-ski research airplane has been made in the Langley 300 MPH 7- by 10-foot tunnel. Hydro-skis are a form of retractable landing gear consisting of planing surfaces which provide acceptable characteristics for aircraft on water, snow, and ice without compromising their flight performance. Tank tests (reference 1) followed by successful full-scale tests (reference 2) of a low-speed amphibian fitted with hydro-skis have shown their feasibility for low-speed aircraft.

The Edo 142 airplane was designed to study the feasibility of using hydro-skis on a jet-propelled high-speed fighter-type airplane. Since the hydro-skis would be fully retracted during high-speed flight, the landing and take-off characteristics were of primary concern.

The present paper contains the results of a low-speed longitudinal and lateral stability and control investigation of a $\frac{1}{5}$ -scale model of the airplane. Results of an investigation to develop a suitable jet-engine air intake for the airplane are also included.

SYMBOLS

The system of axes used, together with an indication of the positive forces, moments, and angles, is presented in figure 1. The symbols used in this paper are defined as follows:

- C_L lift coefficient (Lift/ qS)
- C_X longitudinal-force coefficient (X/qS)
- C_Y lateral-force coefficient (Y/qS)
- C_l rolling-moment coefficient (L/qSb)
- C_m pitching-moment coefficient ($M/qS\bar{c}$)

- C_n yawing-moment coefficient (N/qSb)
- C_D drag coefficient ($-C_X$ when $\psi = 0$)
- X longitudinal force along X-axis, pounds
- Y lateral force along Y-axis, pounds
- Z force along Z-axis (lift equals $-Z$), pounds
- L rolling moment about X-axis, foot-pounds
- M pitching moment about Y-axis, foot-pounds
- N yawing moment about Z-axis, foot-pounds
- q free-stream dynamic pressure, pounds per square foot ($\rho V^2/2$)
- S wing area, square feet
- \bar{c} wing mean aerodynamic chord, feet
- b wing span, feet
- V free-stream velocity, feet per second
- A aspect ratio (b^2/S)
- ρ mass density of air, slugs per cubic foot
- α angle of attack of thrust line, degrees
- ψ angle of yaw, degrees
- i_t angle of incidence of stabilizer with respect to thrust line, degrees
- δ control-surface deflection measured in a plane perpendicular to hinge line
- H total pressure, pounds per square foot
- p static pressure, pounds per square foot
- $C_{l_\psi} = \left(\frac{\partial C_l}{\partial \psi} \right)_\alpha$

$$C_{n_\psi} = \left(\frac{\partial C_n}{\partial \psi} \right)_\alpha$$

$$C_{Y_\psi} = \left(\frac{\partial C_Y}{\partial \psi} \right)_\alpha$$

The subscript α indicates that α was held constant.

Subscripts:

- e elevator
- a aileron
- r rudder
- 0 free-stream conditions
- 1 conditions at duct inlet
- 2 conditions at compressor rake

MODEL AND APPARATUS

The physical characteristics of the $\frac{1}{5}$ -scale model of the Edo 142 airplane are presented in figure 2 and table I and photographs of the model are shown in figure 3. Dimensions of the three slat configurations investigated are given in figure 4; fence dimensions and fence locations are presented in figure 5. A plain sealed aileron was incorporated in the left wing (fig. 2). The ruddervator gap was also sealed. The term ruddervator will be applied to the vee-tail control surfaces that produce the combined effect of elevator and rudder. These same tail surfaces will be referred to as elevators when used only as a longitudinal control and rudders when used only as a directional control. Revisions of the sternpost region of the fuselage and the addition of a water rudder to the model are shown in figure 6.

The afterducting of the jet engine was simulated by the use of an open tube of constant diameter. Fittings of the tail mounting partially blocked the duct in the rear region (fig. 3); therefore, duct tests were made with the tail removed. Pressure rakes made of 0.030-inch steel tubing were located at two fuselage stations (fig. 7), one at the duct inlet and the other at the region of the airplane engine compressor.

The inlet rake consisted of 26 total-pressure tubes and 5 static-pressure tubes; whereas the compressor rake had 24 total-pressure tubes and 12 static-pressure tubes (fig. 8).

The original ramp plan form and the modified ramp which was tested with three different wall heights are shown in figure 9. The low-wall-ramp configuration was obtained by cutting down the high-wall ramp to a flat surface; whereas the medium wall was built-up from the low wall with modeling clay. The ramp floor remained the same throughout the tests.

TESTS

The tests were made in the Langley 300 MPH 7- by 10-foot tunnel at a dynamic pressure of 22.64 pounds per square foot which corresponds to a Mach number of 0.12 and a Reynolds number of 1.16×10^6 based on the mean aerodynamic chord of 1.35 feet.

Most of the force tests were made with the original duct ramp incorporated on the model. The effect of modifying the ramp on the model stability and control characteristics is believed to be small.

Jet-engine air-inlet velocities were varied from 1.70 to 0.50 free-stream velocity by using orifice plates at the rear of the duct. Most of the duct surveys were made at an inlet-velocity ratio near 0.80, the estimated value required for the jet engine (Westinghouse J-34-WE-22) of the airplane in the landing speed range.

CORRECTIONS

The angle of attack, drag coefficients, and pitching-moment coefficients have been corrected for jet-boundary effects determined by methods of reference 3 based on unswept wings. The effects of wing sweep on the corrections have been found to be negligible (reference 4). The model coefficients have been corrected for blocking by the model and its wake by the methods of reference 5.

Tare corrections resulting from the support strut have not been applied since experience on similar models indicates that these corrections would be small except for the drag. Estimates made from previous investigations of similar complete models in the 300 MPH 7- by 10-foot tunnel indicate that the drag coefficients presented for the

$\frac{1}{5}$ -scale model will be lower by about 0.01 if the effects of the model support struts are considered.

Horizontal buoyancy on the model and tunnel-air-flow misalignment have also been accounted for in the computation of the test data. The ram-recovery ratios have been computed from the average value of the total-pressure readings.

RESULTS AND DISCUSSION

The figures in which the results are presented are summarized in the following table:

	Figure
Longitudinal Stability and Control:	
Effect of tail incidence	10
Elevator effectiveness	11
Neutral point location	12
Effect of stall-control devices	13
Effect of alighting gear	14
Lateral Stability:	
Parameters	15
Characteristics in yaw range	16
Directional Control:	
Rudder effectiveness	17
Lateral Control:	
Aileron characteristics in pitch	18
Aileron characteristics in yaw	19
Pressure Recovery:	
Ram-recovery-ratio contours at inlet	20
Variation of inlet ram-recovery ratio with inlet velocity ratios	21
Variation of ram-recovery and velocity ratios at the inlet with angle of attack	22
Ram-recovery-ratio contours at compressor	23
Variation of ram-recovery and velocity ratios at compressor with angle of attack	24

Longitudinal Stability and Control

Results of the tail incidence and elevator tests, figures 10 and 11, respectively, indicate that the model possesses large longitudinal stability throughout the lift-coefficient range for the normal center of gravity. Elevator-fixed neutral points of the model determined from the stabilizer tests are presented in figure 12. The power effect of the jet engine which has been estimated from thrust consideration only (fig. 12) adds positive static margin because of the relatively large vertical distance of the thrust axis above the center of gravity.

At high lift coefficients, the model became very stable, figures 10 and 11, resulting in reduced effectiveness of the elevators which limited the trim lift coefficient to 1.09 for the model with the center of gravity at normal position (0.25 M.A.C.). The landing speed of the full-scale airplane with a wing loading of 41 pounds per square foot is thus estimated to be 121 miles per hour, Reynolds number differences between the full-scale airplane and the model being neglected. A maximum trim lift coefficient of 1.2, corresponding to a landing speed of 115 miles per hour (fig. 11(b)), could be obtained at a more rearward center-of-gravity position, 0.40 M.A.C., where the model had a static margin not less than 0.04 M.A.C., figure 12. It may not be desirable however, to move the center of gravity to the rearward position because of directional-stability requirements which will be discussed later. With the normal center of gravity, a maximum trim lift coefficient, 1.17, could be obtained by extending the original slat inboard 12 percent semispan without the fence (fig. 11(c)). Longitudinal stability and control parameters of the model are presented in table II.

Stall-Control Devices

In an attempt to increase the maximum trim lift coefficient obtainable on the airplane by delaying the stable break of the pitching moment to higher lift coefficients, the effect of varying the position and size of the stall-control devices was investigated (fig. 13).

The model without stall-control devices and the model with the $0.32\frac{b}{2}$ slat and fence at $0.49\frac{b}{2}$ possessed a region of neutral stability in the upper part of the lift-coefficient range and had relatively low maximum lift coefficient. The addition of a fence alone had only a slight effect on maximum lift coefficient. The $0.49\frac{b}{2}$ slat resulted in appreciable increases in maximum lift with slight decreases in drag at angles up to about 8° . Above 8° , the drag rise and the stable break in the pitching moment were delayed to higher lift coefficients with the addition of the slat. As the slat span was increased to $0.75\frac{b}{2}$

maximum lift increased, while the drag rise and stable break of the pitching moment were delayed.

The addition of the fence to the wing with the slat affected the model characteristics only slightly and resulted in very little change in maximum lift coefficient.

Alighting Gear

The effect of lowering the various components of the alighting gear on the aerodynamic characteristics of the test model is presented in figure 14. The data show that lowering the gear generally increased maximum lift by a small increment, with the highest maximum lift occurring with both skis down and ski wells filled with modeling clay and faired smooth to hull-bottom contours. Except near the stall, the pitching moment generally became slightly more negative with extension of the gear; very little elevator deflection would be required, however, to counteract the trim change. The drag increment due to lowering the gear was positive for lift coefficients below 0.9. Above about 0.9 lift coefficient, the drag increment was negative because of the increased lift due to lowering the gear. Fairing the main ski well reduced the drag coefficient considerably; however, fairing the tail ski well had only a slight effect.

Lateral Stability

The static lateral-stability parameters determined from tests at angles of yaw of 0° and 5° are plotted against lift coefficient in figure 15 for the wing alone with tip floats, the model with tail off, and with various configurations of the complete model. The results of yaw tests at several angles of attack for several model configurations are presented in figure 16.

The variation of effective dihedral for the wing alone with tip floats generally agrees closely with estimates determined from references 6 and 7. As seen in figure 15(a), the addition of the fuselage to the wing resulted in a positive increment in C_{l_ψ} (as might be expected for a high-wing model configuration with extensive fuselage side area), but did not have a large effect on the variation of effective dihedral with lift coefficient. The addition of the vee tail to the model resulted in a large increment in C_{l_ψ} , particularly at low lift coefficients. The maximum value of C_{l_ψ} occurred at a lift coefficient of about 0.8 and corresponds to an effective dihedral of 28° on a plain

untapered wing of aspect ratio 6. The addition of an end plate, obtained by filling in the region between the tip float and the extended skid, generally decreased the variation of $C_{L_{\psi}}$ with C_L . The data of reference 8 indicate that an increase in Reynolds number corresponding to flight would increase the maximum effective dihedral by extending the range of increasing $C_{L_{\psi}}$ with C_L to higher lift coefficients and thus delay and possibly reduce the decreasing tendencies of $C_{L_{\psi}}$ exhibited by the data at high lift coefficients.

The model, as originally tested (fig. 2), had practically neutral directional stability in the yaw range of $\pm 5^\circ$ at low angles of attack as shown in figure 16. Tail-off tests, figure 17, also showed the largest instability in the same yaw range and indicated that the contribution of directional stability from the tail was about constant throughout the yaw range tested. Observation of the air flow over the hull by means of wool tufts indicated no separation, but showed a region of rough flow near the sternpost where the trailing-edge angle was large (fig. 6). The hull bevel probably produced the instability in a manner somewhat similar to that by which a bevel of about the same trailing-edge angle on a control surface produces a hinge-moment overbalance through a small angle-of-attack range.

The directional stability of the model in the low yaw range increased with angle of attack; above an angle of attack of 10° , the yaw range of reduced stability was absent.

An attempt was made to alleviate the directional instability in the low angle-of-attack range and yaw range by building up the rear portion of the hull as shown in figure 6. With the built-up trailing-edge configuration the model was directionally stable, figure 16, but the stability was still considerably less in the low yaw-angle range compared to that of the high yaw-angle range. Addition of a water rudder improved the directional stability in the low yaw-angle range. With the faired water rudder (fig. 6), the directional instability was worse than with the original configuration (fig. 16(a)).

Although the effective dihedral was large because of the vee tail, references 9 and 10 indicate that the effect might not prove detrimental for the configuration with blunted afterbody (depending on the mass distribution of the Edo airplane) because of the over-all large directional stability. Reference 11 indicates that, at landing approach speeds, effective dihedral high enough to produce oscillatory instability on one airplane could be tolerated by pilots (that is, would not be dangerous to fly but would not necessarily be desirable or pleasant).

Directional Control

The effects of rudder deflection on the aerodynamic characteristics of the model in yaw are given in figure 17. The data are presented for angles of attack of 0° to 12° , with corresponding elevator trim angles of 0° and -20° . Rudder effectiveness was less at the larger elevator trim angles, but was still adequate to trim the model to an angle of yaw of about 15° . The changes in pitching moment resulting from rudder deflections were generally small and the maximum spread of the curves indicates that the largest change in elevator angle for trim would be about 2° .

Although rudder deflections required for trim at small yaw angles (5° to -5°) would be different than indicated by figure 15 for the model with a revised rearward portion of the hull, the rudder deflections required for higher yaw angles would be similar because the change in yawing moment caused by hull afterbody revisions generally occurred only in the yaw range of $\pm 5^\circ$. Rudder effectiveness generally varied linearly with rudder deflection for the range of rudder angles tested and showed no tendency to decrease at the high rudder angles.

Lateral Control

The effect of aileron deflection on the aerodynamic characteristics of the original model is presented in figure 18; these data were obtained with only the left aileron deflected. The aileron was effective up to and beyond the angle of attack for maximum lift coefficient, about 22° . The aileron effectiveness was about constant for negative aileron deflections through the angle-of-attack range up to 22° . For positive deflections aileron effectiveness dropped off slightly at angles of attack approaching the stall. The aileron effectiveness generally held to high deflections throughout a large part of the angle-of-attack range and indicated that deflections larger than those tested would produce satisfactory increments of roll.

Favorable yawing moments accompanying aileron deflection occurred for angles of attack less than about 3° . This favorable effect may in part be attributed to an end-plate effect caused by the tip floats as noted in reference 12. Part of the effect, however, may be attributed to sidewash induced at the tail by aileron deflection. At high angles of attack, unfavorable yawing moments accompanied aileron deflection. Because the aileron effectiveness is not reduced with angle of yaw, according to figure 19, and because the model can be made to possess large directional stability throughout the entire yaw range by blunting of the hull sternpost region, the amount of unfavorable yaw due to aileron deflection present will have only a slight effect on static roll effectiveness, although the model had large amounts of

effective dihedral. The aileron roll effectiveness parameter $C_{l\delta}$ obtained in the vicinity of $\alpha = 0$ shows good agreement with theory of reference 13. The measured value obtained for $C_{l\delta}$ was 0.0014 compared to the theory which gives a value for $C_{l\delta}$ of 0.0013. The increased value for the experimental results can be attributed to an end-plate effect of the tip floats (reference 12).

Duct Pressure Recovery

The ram recovery characteristics at the duct inlet are presented in figure 20 for the original ramp and for the modified ramp with high ramp walls. The data show that the original ramp had large ram-recovery-ratio losses in the lower region of the inlet caused by a building-up of the boundary layer. This condition occurred even at low angles of attack.

It was expected that because of this large boundary layer there would be separation on the lower wall of the diffuser, which had a sharp radius of curvature (fig. 7). Reference 14, which is a study of the effects of various ramp shapes on the ram-recovery characteristics, indicated that for over-all ram-recovery efficiency the trumpet-shaped ramp plan form would be more desirable than the one originally tested.

The model was therefore modified to incorporate the ramp plan form as shown in figure 9. The ram-recovery contours of the modified ramp generally had good recovery in the lower region of the inlet throughout the angle-of-attack range. This good recovery near the ramp floor resulted from strong vortices emanating from the deep walls which were effective in preventing thick boundary layer on the floor. With the strong vortices, however, large losses occurred in the region just below the lip. The inlet ram-recovery-ratio variation with inlet-velocity ratio for several angles of attack of the model is shown in figure 21 for the original and modified high-wall ramp. Although the over-all ram recovery was slightly less for the modified ramp, the recovery pattern with lower losses on the ramp floor is probably more desirable. The large ram-recovery loss at an angle of attack of 20° for the high-wall ramp resulted from losses in the upper part of the duct inlet as mentioned previously for low angles. An angle of attack of 20° , however, is beyond the range of α for maximum trim lift coefficient. The variation of inlet ram-recovery ratio and inlet-velocity ratio with angle of attack is shown in figure 22 for the original ramp and modified high-wall ramp. At low angles of attack up to 8° the ram recovery was about the same for both ramps, but at angles

above 8° the ram recovery of the modified ramp gradually became less. Both ramps possessed a sharp decrease in ram recovery between angles of attack of 16° and 20° . The velocity ratios were about the same at low angles; however, the modified-ramp velocity ratio became less at higher angles.

It was believed that the total-pressure readings might have been in error due to cross flow in the vortex region of the duct. A shielded total-pressure tube was used in an attempt to find any error that existed. The data showed that the original rake pressures were at most about 3 percent low.

Although the data are not presented, several lip plan-form shapes were tested which showed very little or no improvement in the ram recovery characteristics.

The ram recovery characteristics at the compressor entrance are presented in figure 23 for the modified ramp plan form with three wall heights. The variation of ram-recovery ratio and velocity ratio with angle of attack is shown in figure 24. The high-wall contours show favorable over-all ram recovery decreasing with angle of attack with the greater losses in the upper region of the duct corresponding to the vortex losses at the duct inlet. By reducing the wall height to the medium wall, a more uniform flow distribution was noted and was evidently caused by the reduced strength of the vortex. When the wall height was reduced even further the vortex strength was reduced and was incapable of sweeping the boundary layer from the floor; thus, the losses in the lower region became overly large.

The trumpet-shaped ramp with medium-height walls appeared to give the most uniform flow distribution and the highest recovery at the location of the compressor entrance of any configuration tested.

CONCLUSIONS

The results of an investigation in the Langley 300 MPH 7- by 10-foot tunnel to determine the low-speed stability and control and the jet-engine duct-inlet pressure recovery characteristics of a $\frac{1}{5}$ -scale model of the Edo 142 hydro-ski research airplane indicate the following conclusions:

1. The model had elevator-fixed static longitudinal stability amounting generally to a static margin of about 0.19 mean aerodynamic chord throughout most of the lift-coefficient range and became extremely stable near the stall.

2. The maximum trim lift coefficient available from the elevators was 1.09 and was increased to 1.2 by extension of the leading-edge slat inboard.

3. The model had approximately neutral static directional stability over the yaw range of $\pm 5^\circ$ at low angles of attack. It could be made stable by blunting the rearward end of the hull.

4. The effective dihedral of the model was high throughout the lift-coefficient range mainly because of the large vee tail.

5. The effectiveness of the rudder (rudervators) was adequate to trim the model through the yaw range of $\pm 15^\circ$ at both low and high up-elevator (ruddervator) trim angles.

6. The aileron effectiveness was satisfactory up to and beyond the angle of attack for maximum lift coefficients.

7. Of several configurations of the jet-engine duct inlet, which was located on top of the fuselage, a duct with a trumpet-shaped ramp with medium-height walls appeared to give the most uniform flow distribution and the highest ram recovery at the location of the engine compressor.

Langley Aeronautical Laboratory
National Advisory Committee for Aeronautics
Langley Field, Va.

REFERENCES

1. Wadlin, Kenneth L., and Ramsen, John A.: Tank Investigation of the Grumman JRF-5 Airplane Fitted with Hydro-Skis Suitable for Operation on Water, Snow, and Ice. NACA RM L9K29, 1950.
2. Anon.: Summary Report on USAF Project MX-940. Rep. 2719, Edo Corp., April 5, 1949.
3. Gillis, Clarence L., Polhamus, Edward C., and Gray, Joseph L., Jr.: Charts for Determining Jet-Boundary Corrections for Complete Models in 7- by 10-Foot Closed Rectangular Wind Tunnels. NACA ARR L5G31, 1945.
4. Polhamus, Edward C.: Jet-Boundary-Induced-Upwash Velocities for Swept Reflection-Plane Models Mounted Vertically in 7- by 10-Foot, Closed, Rectangular Wind Tunnels. NACA TN 1752, 1948.
5. Herriot, John G.: Blockage Corrections for Three-Dimensional-Flow Closed-Throat Wind Tunnels, with Consideration of the Effect of Compressibility. NACA Rep. 995, 1950.
6. Toll, Thomas A., and Queijo, M. J.: Approximate Relations and Charts for Low-Speed Stability Derivatives of Swept Wings. NACA TN 1581, 1948.
7. Goodman, Alex, and Brewer, Jack D.: Investigation at Low Speeds of the Effect of Aspect Ratio and Sweep on Static and Yawing Stability Derivatives of Untapered Wings. NACA TN 1669, 1948.
8. Neely, Robert H., and Conner, D. William: Aerodynamic Characteristics of a 42° Swept-Back Wing with Aspect Ratio 4 and NACA 64-112 Airfoil Sections at Reynolds Numbers from 1,700,000 to 9,500,000. NACA RM L7D14, 1947.
9. McKinney, Marion O., Jr.: Experimental Determination of the Effects of Dihedral, Vertical-Tail Area, and Lift Coefficient on Lateral Stability and Control Characteristics. NACA TN 1094, 1946.
10. Campbell, John P., and Seacord, Charles L., Jr.: The Effect of Mass Distribution on the Lateral Stability and Control Characteristics of an Airplane as Determined by Tests of a Model in the Free-Flight Tunnel. NACA Rep. 769, 1943. (Formerly NACA ARR 3H31.)

11. Kauffman, William M., Liddell, Charles J., Jr., Smith, Allan, and Van Dyke, Rudolph D., Jr.: An Apparatus for Varying Effective Dihedral in Flight with Application to a Study of Tolerable Dihedral on a Conventional Fighter Airplane. NACA Rep. 948, 1949.
12. Riebe, John M., and Watson, James M.: The Effect of End Plates on Swept Wings at Low Speed. NACA TN 2229, 1950.
13. Lowry, John G., and Schneiter, Leslie E.: Estimation of Effectiveness of Flap-Type Controls on Sweptback Wings. NACA TN 1674, 1948.
14. Frick, Charles W., Davis, Wallace F., Randall, Lauros M., and Mossman, Emmet A.: An Experimental Investigation of NACA Submerged-Duct Entrances. NACA ACR 5120, 1945.

TABLE I

CHARACTERISTICS OF $\frac{1}{5}$ -SCALE MODEL OF THE EDO 142 AIRPLANE

[Original configuration]

General:

Distance from normal center of gravity to rudder	
hinge at M.A.C., inches	43.2
Span (including tip floats), inches	69.0
Length, inches	101.7
Height, inches	24.6

Wing:

Span (no floats), inches	64.8
Chord (parallel to airplane center line), inches	16.2
Aspect ratio	4.0
Taper ratio	1.0
Incidence, degrees	2.5
Dihedral, degrees	-2.0
Sweepback, degrees	35.0
Airfoil section (normal to leading edge)	NACA 64 ₁ -412

Slat (fixed, external):

Chord, inches	1.93
Span (exposed 18.5 in.), inches	20.27

Empennage:

Span (true), inches	40.2
Chord (constant), inches	10.99
Incidence, degrees	1.25
Dihedral, degrees	45
Airfoil Section	NACA 64-009
Sweepback, degrees	35

Fuselage:

Width (max.), inches	7.0
Height to top of canopy, inches	16.7
Length (without empennage), inches	92.9
Duct (max. diam.), inches	4.5



TABLE I

CHARACTERISTICS OF $\frac{1}{5}$ -SCALE MODEL OF THE EDO 142 AIRPLANE - Continued

Areas:

Wing (total), square feet	7.29
Aileron (one), square feet	0.393
Slats (each)(exposed 0.206 sq ft), square feet	0.271
Stabilizer, square feet	2.22
Ruddervator (each), square feet	0.32
Stabilizer (horizontal projection), square feet	2.17
Stabilizer (vertical projection), square feet	1.08
Duct entrance, square feet	0.0521

Alighting Gear:

Main Ski:

Length, inches	24.2
Beam, inches	4.4
Area (projected), square feet	0.664

Tail Ski:

Length, inches	11.50
Beam, inches	2.09
Area (projected), square feet	0.150

Tip Float:

Length, inches	26
Beam, inches	4.1

Aileron:

Span, inches	14
Area, square feet	0.393
Chord (perpendicular to hinge line), inches	3.32

Fence:

Span (total), inches	18.36
Height (constant), inches	0.95

Tip Skid:

Boom length, inches	14.0
Skid length, inches	3.70
Skid beam, inches	1.22



TABLE I

CHARACTERISTICS OF $\frac{1}{5}$ -SCALE MODEL OF THE EDO 142 AIRPLANE - Concluded

Ruddervator:

Span (true), inches	15.3
Span (horizontal), inches	10.8
Span (vertical), inches	10.8
Chord (perpendicular to hinge line), inches	2.70

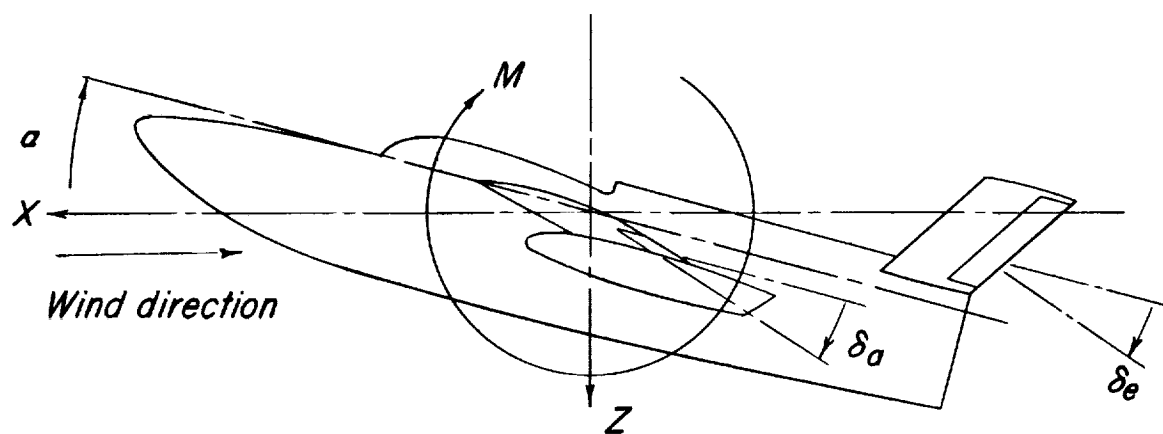
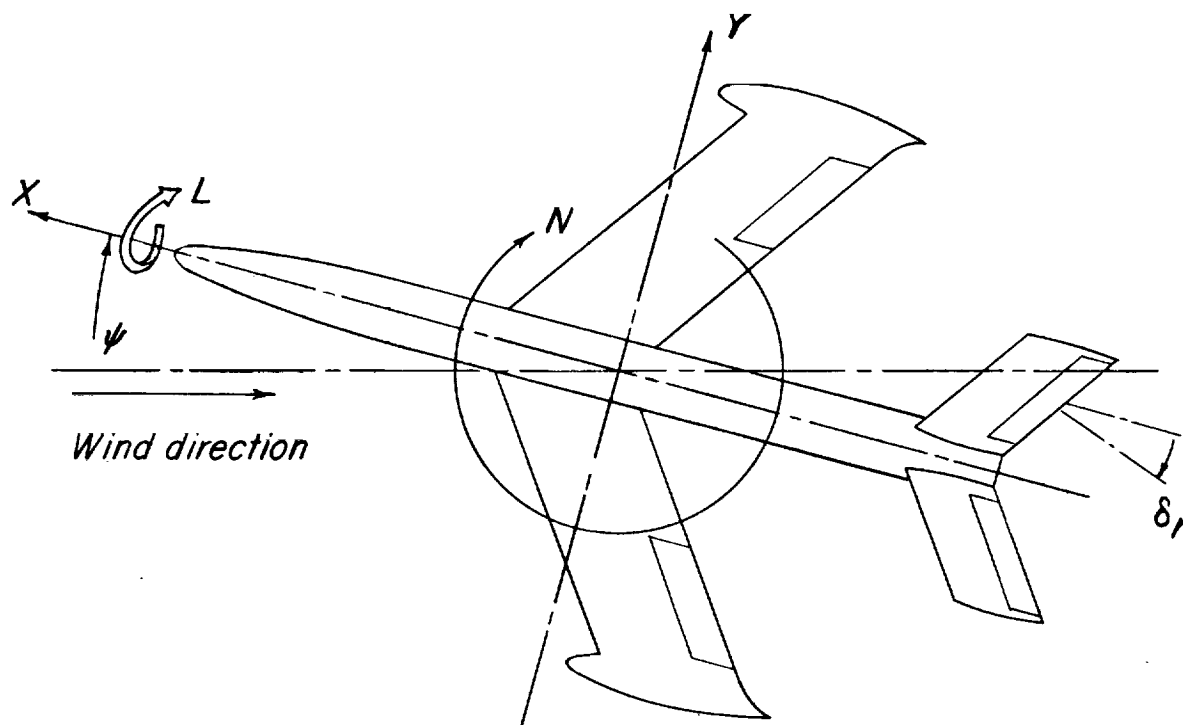


TABLE II
 STABILITY AND CONTROL CHARACTERISTICS OF THE $\frac{1}{5}$ -SCALE MODEL
 OF THE EDO 142 HYDRO-SKI RESEARCH AIRPLANE
 [Center of gravity at 0.25 M.A.C.]

Configuration	$\frac{\partial C_L}{\partial \alpha}$	$\frac{\partial C_m}{\partial i_t}$	$\frac{\partial C_m}{\partial \delta_e}$	$\frac{a}{b}$
Complete model (Gear up)	0.079	-0.0235	-0.0157	0.67
Wing and tip floats Wing alone (Theory)	.071 .062	-----	-----	-----
Model without tail	.072	-----	-----	-----

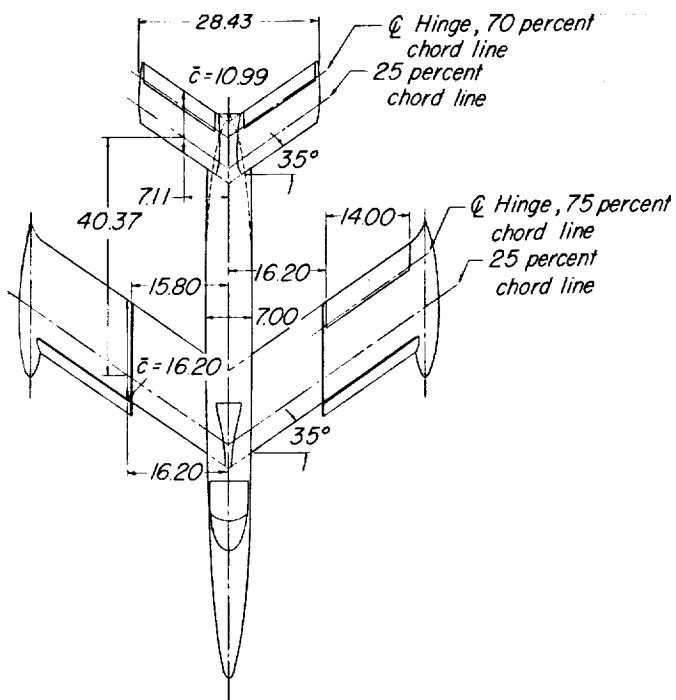
Configuration	α (deg)	$\frac{\partial C_n}{\partial \psi}$		$\frac{\partial C_l}{\partial \psi}$		$\frac{\partial C_n}{\partial \delta_r}$ $\psi = 0$	$\frac{\partial C_l}{\partial \delta_a}$ $\psi = 0$	$\frac{\partial C_n}{\partial \delta_a}$ $\psi = 0$
		Tail on	Tail off	Tail on	Tail off			
Complete model (Original condition)	0	-0.0007	0.0053	0.0034	0.0016	-0.0041	0.0015	0.0010
Complete model (Original condition)	12	-.0018	.0023	.0049	.0040	-.0020	.0014	-.0003
Complete model (Original condition)	20	-.0024	.0018	.0040	.0045	-----	.0013	-.0035
Complete model (Blunted fuselage)	0	-.0011	-----	.0041	-----	-----	-----	-----
Complete model (Blunted fuselage)	12	-.0021	-----	.0055	-----	-----	-----	-----
Complete model (Blunted fuselage and water rudder)	0	-.0015	-----	.0049	-----	-----	-----	-----

NACA



View through X-Z plane

Figure 1.- System of stability axes. Positive directions of forces, moments, and deflections are indicated by arrows.



TABULATED DATA

Areas

Wing	7.29 sq ft
Aileron	3.93 sq ft
Slats, each	2.06 sq ft
Stabilizer (horizontal projection)	2.17 sq ft
Stabilizer (vertical projection)	1.08 sq ft

Wing Characteristics

Taper ratio	1.00
Aspect ratio	4.00
Airfoil section	NACA 64 ₁ -412

Vee Tail Characteristics

Taper ratio	1.00
Airfoil section	NACA 64 -009

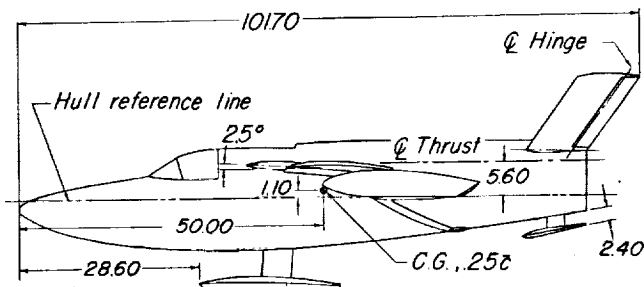
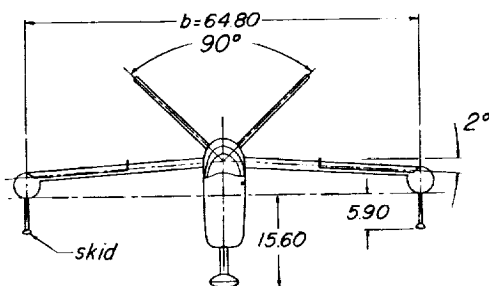
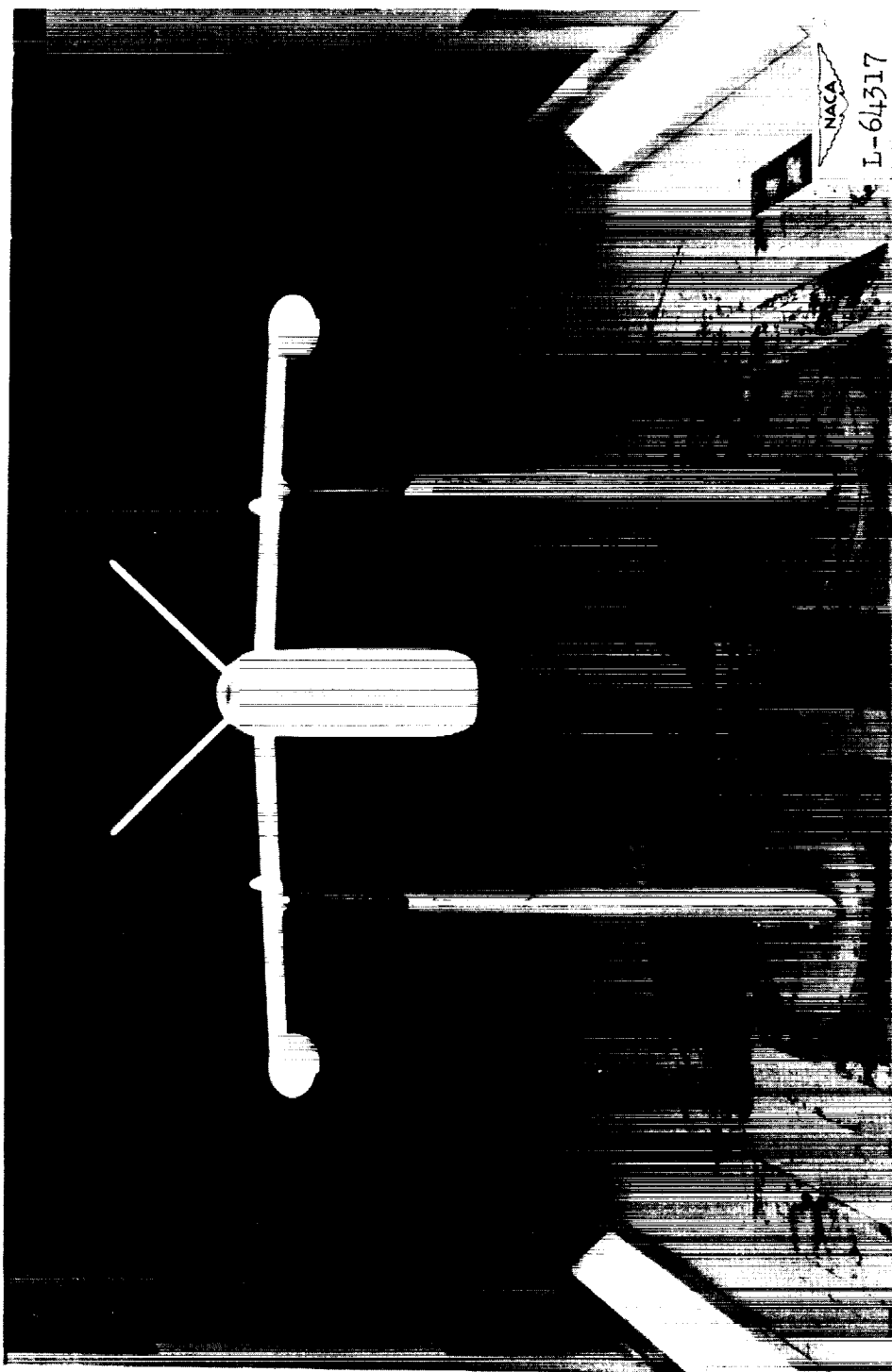


Figure 2.- Three-view drawing of the $\frac{1}{5}$ -scale model of the Edo 142 airplane. All dimensions are in inches.



(a) Front view.

Figure 3.- The $\frac{1}{5}$ -scale model of the Edo 142 airplane tested in the Langley 300 MPH 7- by 10-foot tunnel.



(b) Rear view.

Figure 3.- Continued.



(c) Side view.

Figure 3.- Concluded.

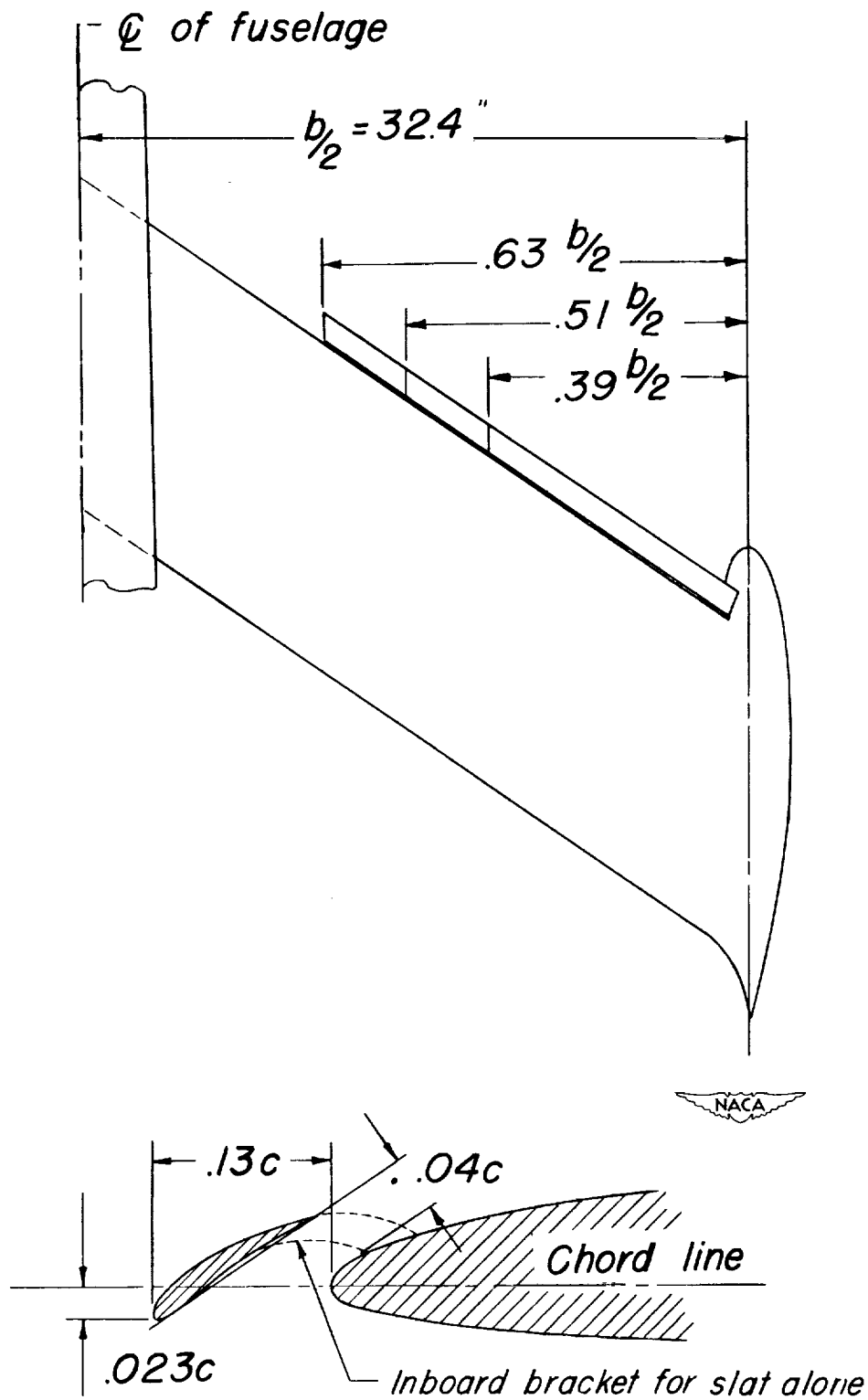


Figure 4.- Details of slats investigated.

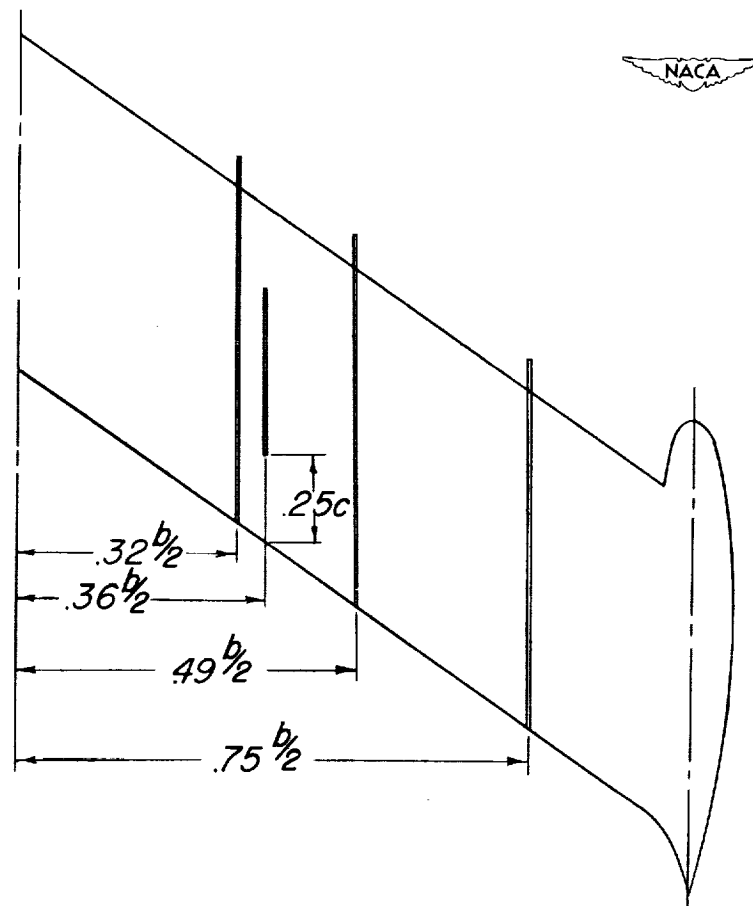
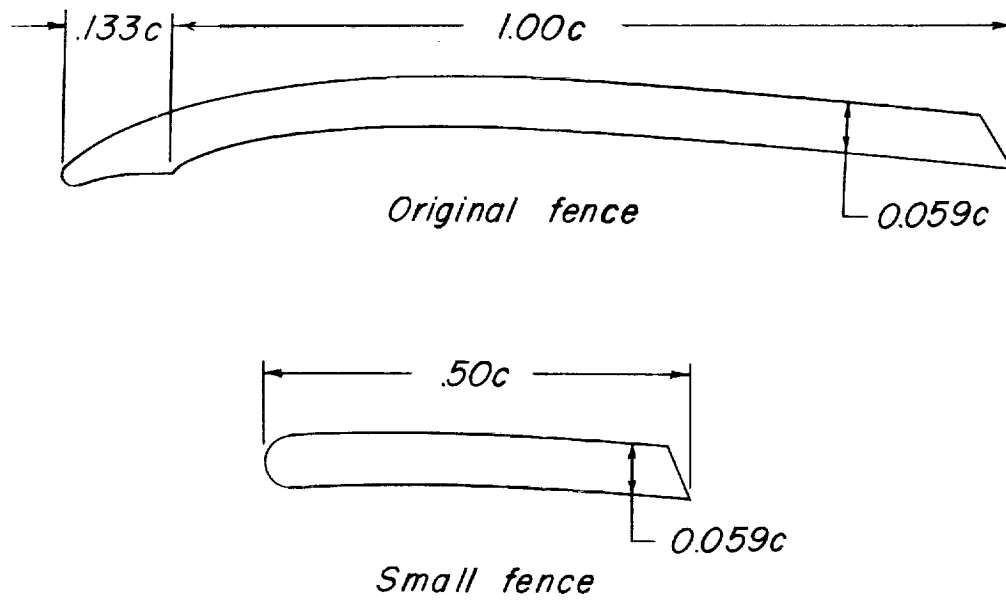


Figure 5.- Details of fences and fence locations.

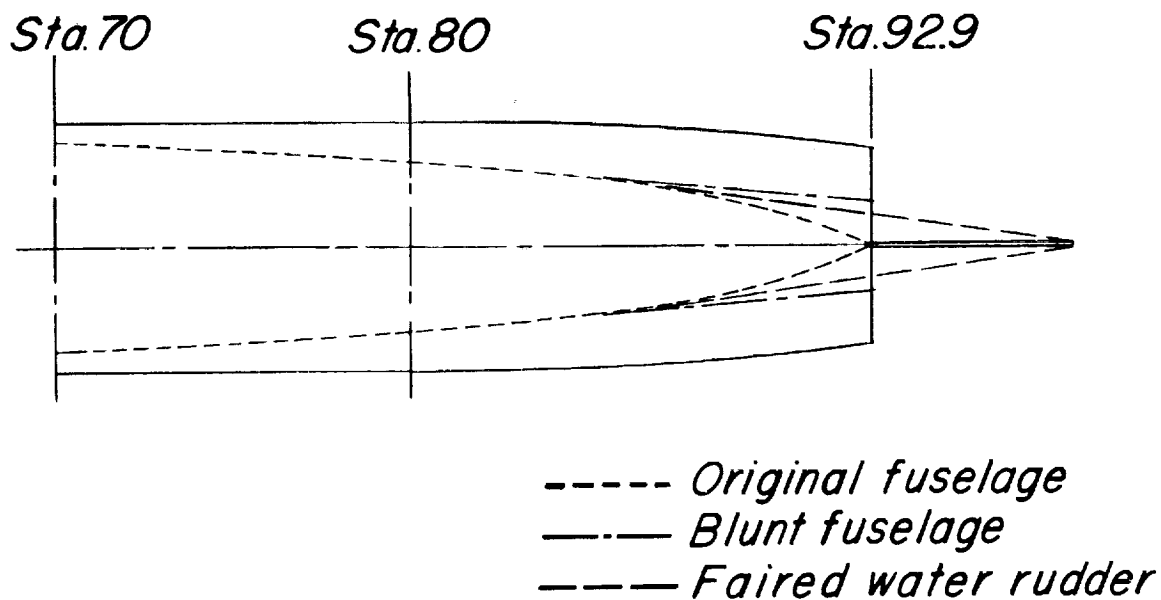
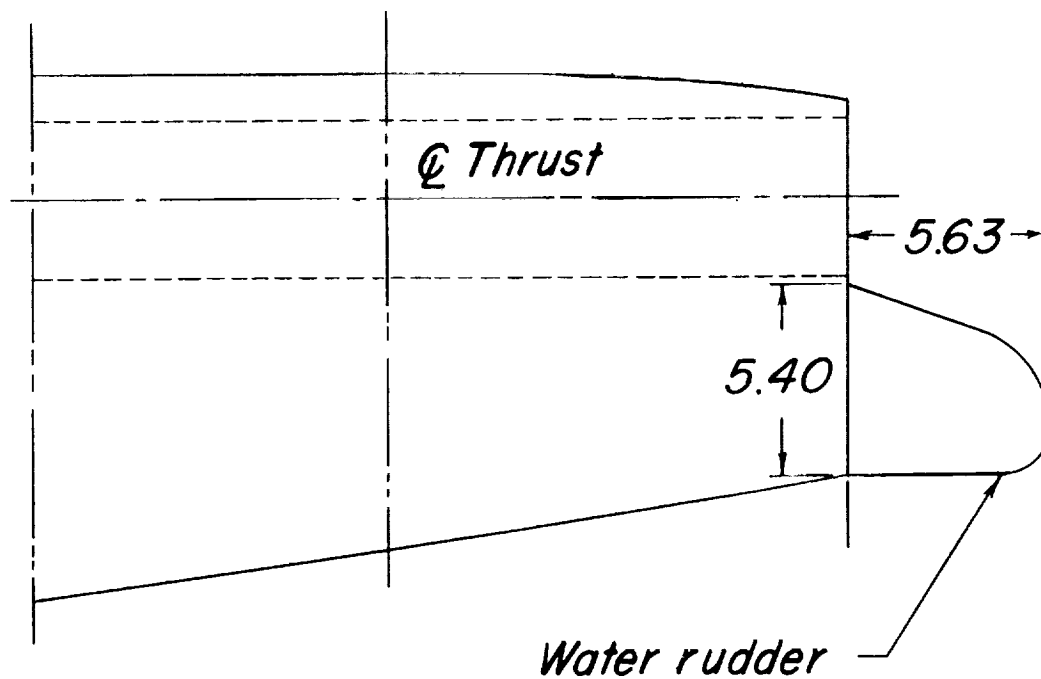


Figure 6.- Details of fuselage sternpost region revisions. All dimensions are in inches.

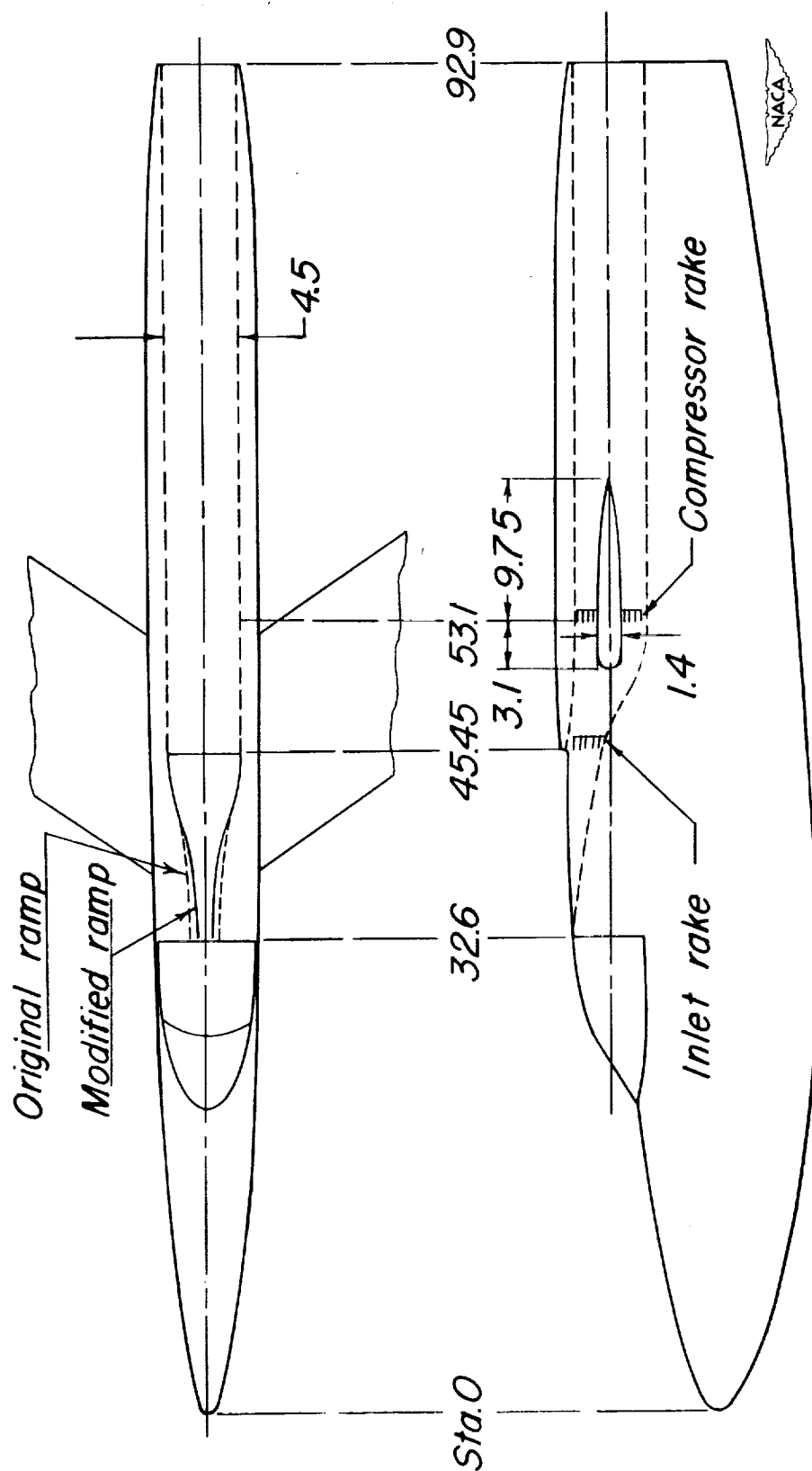
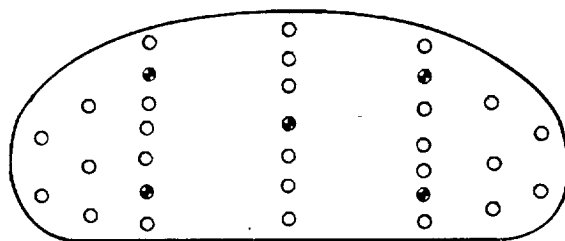
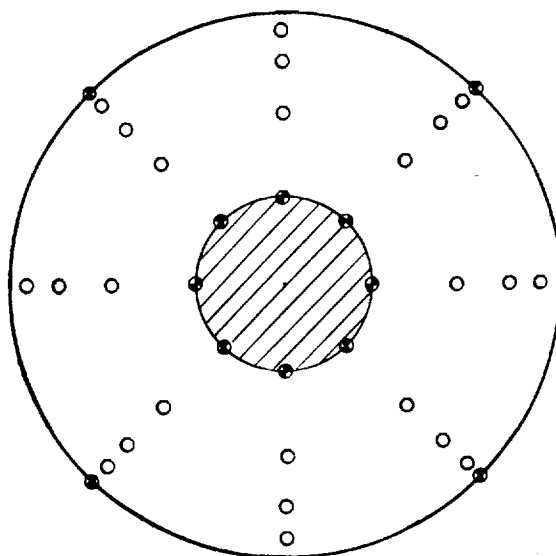


Figure 7.- Schematic drawing showing general arrangement of duct and duct survey rakes. All dimensions are in inches.



*Inlet rake
Station 45.45
Area 7.5 sq in.*

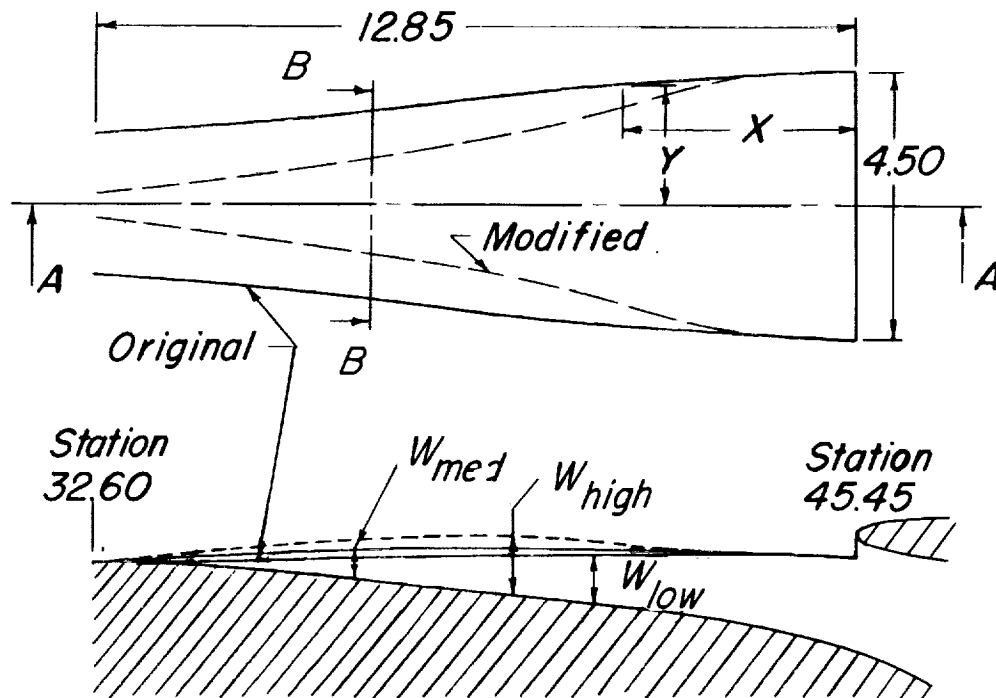
- *Total head tube*
- *Static tube*



*Compressor rake
Station 53.1
Area 14.16 sq in.*



Figure 8.- Details of survey rakes used in pressure studies.

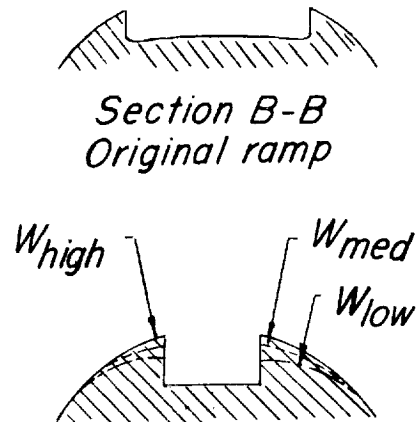


Section A-A



Ramp and Ramp
Wall coordinates

X	Y _{orig}	Y _{mod}	W _{orig}	W _{high}	W _{low}	W _{med}
0	2.25	2.25	1.65	1.65	1.65	1.65
1	2.23	2.25	1.38	1.38	1.38	1.38
2	2.20	2.18	1.16	1.16	1.16	1.16
4	2.11	1.68	.86	1.11	.86	.95
6	1.86	1.14	.64	1.04	.64	.74
8	1.62	.83	.42	.77	.42	.51
10	1.14	.57	.19	.45	.21	.25
12	1.44	.30	.07	.13	.08	.08
12.85	1.22	.19	0	0	0	0



Section B-B
Revised ramp

Figure 9.- Original and modified ramps tested. All dimensions are in inches.

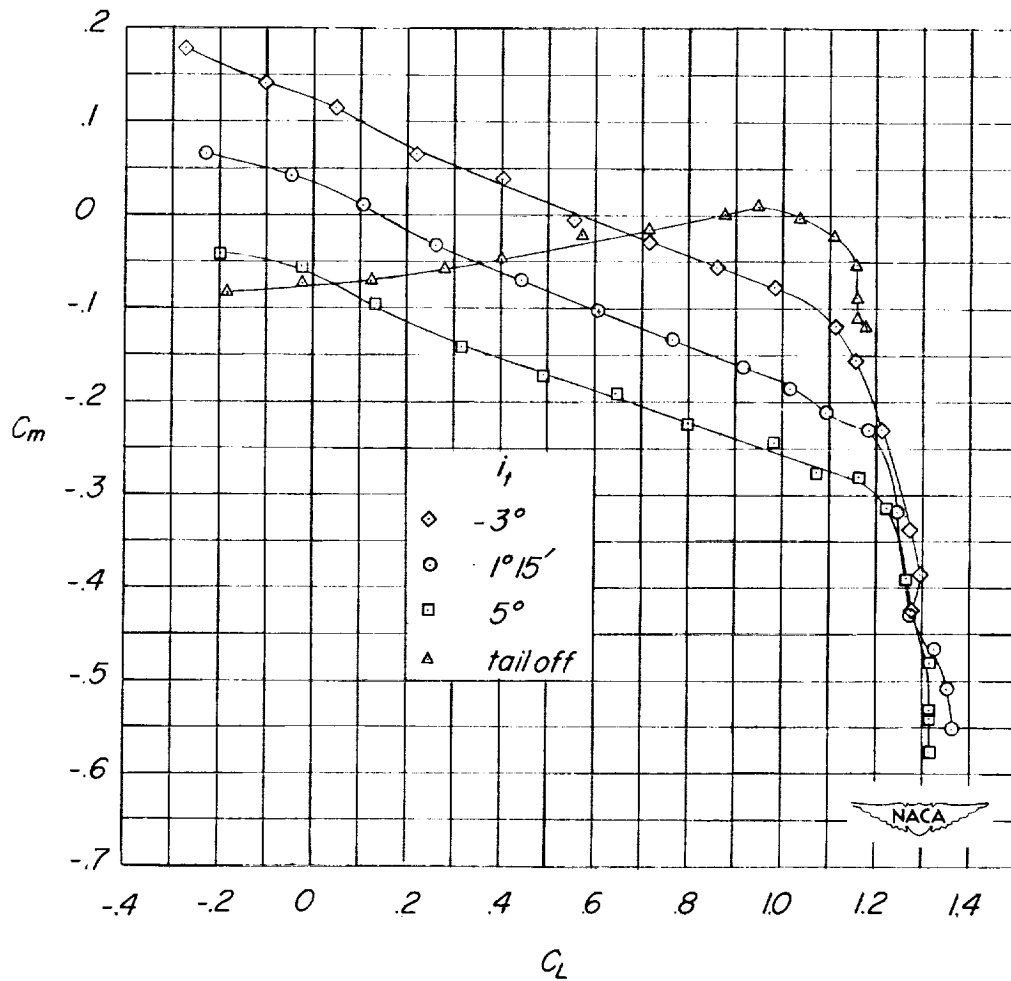


Figure 10.- The effect of tail incidence on the aerodynamic characteristics of the test model. Center of gravity at 0.25 M.A.C.

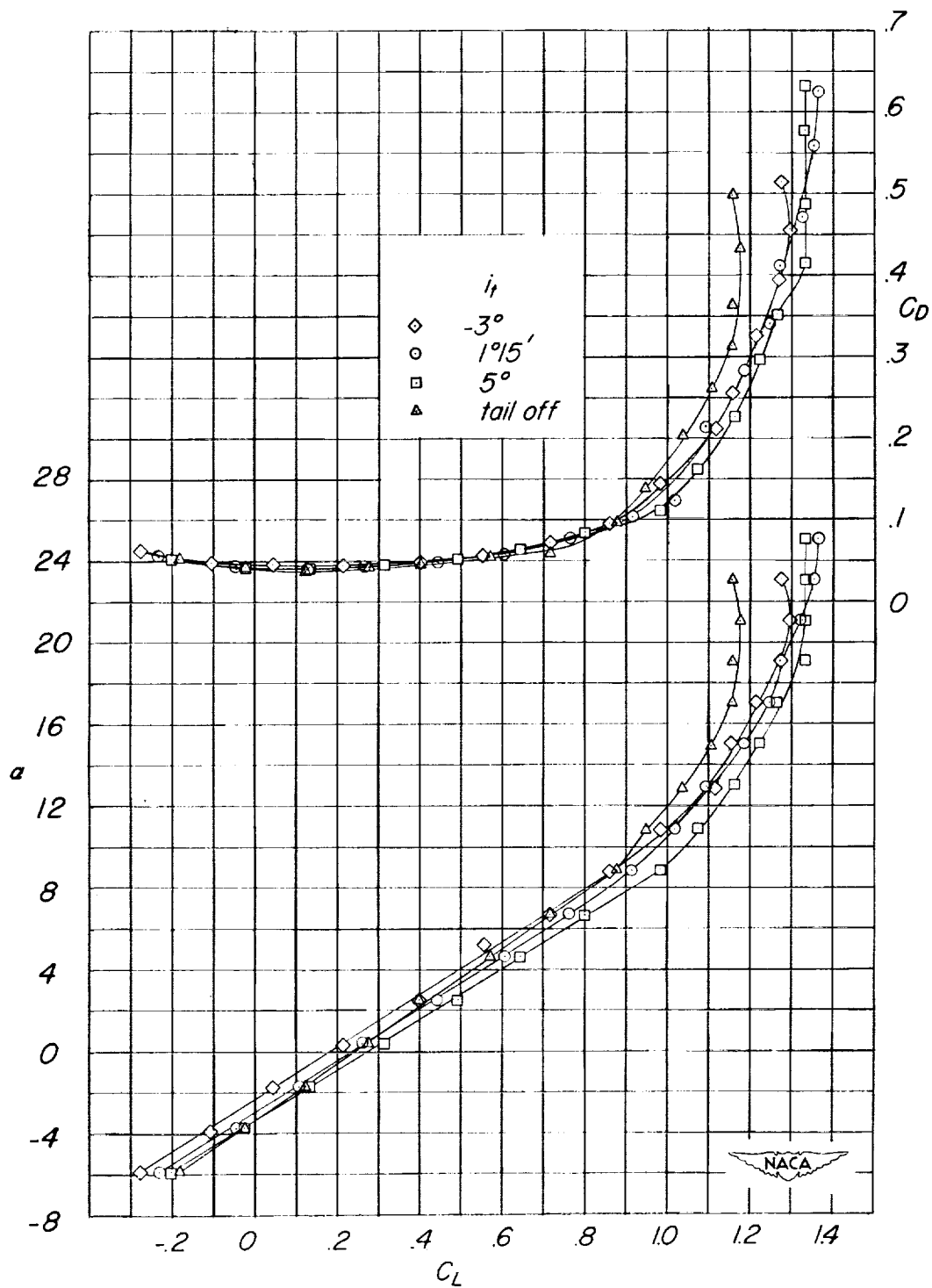
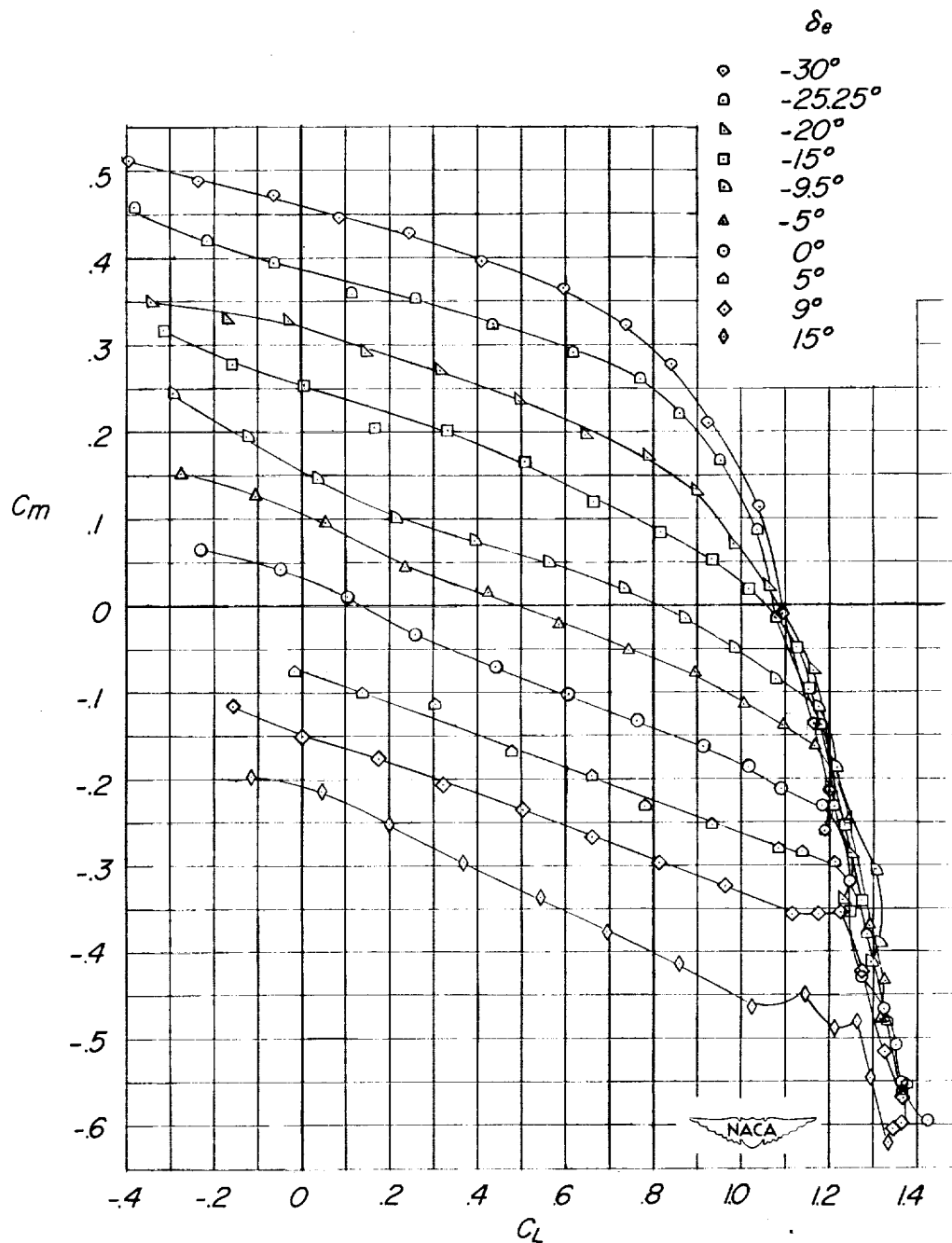
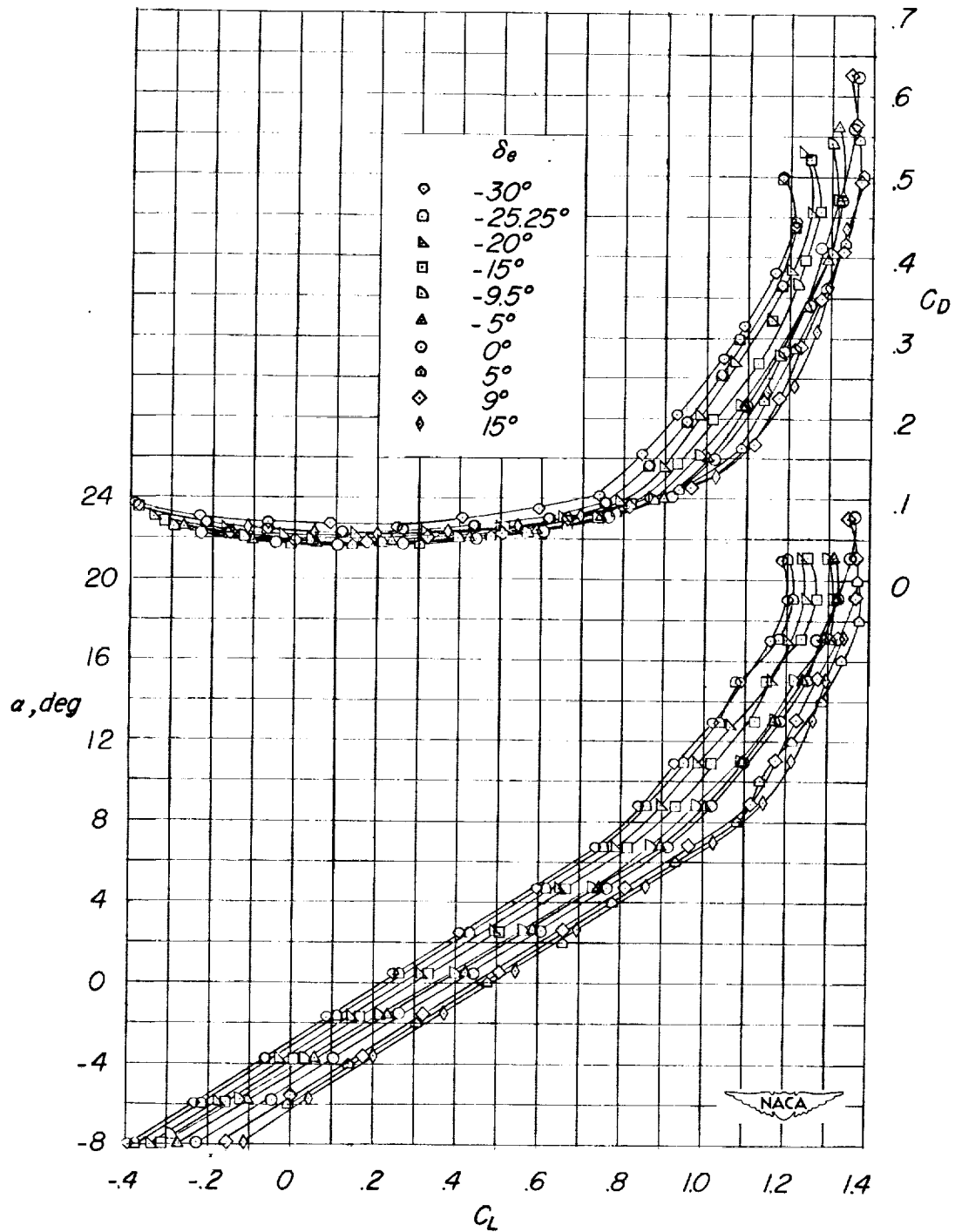


Figure 10.- Concluded.



(a) Center of gravity at 0.25 M.A.C.

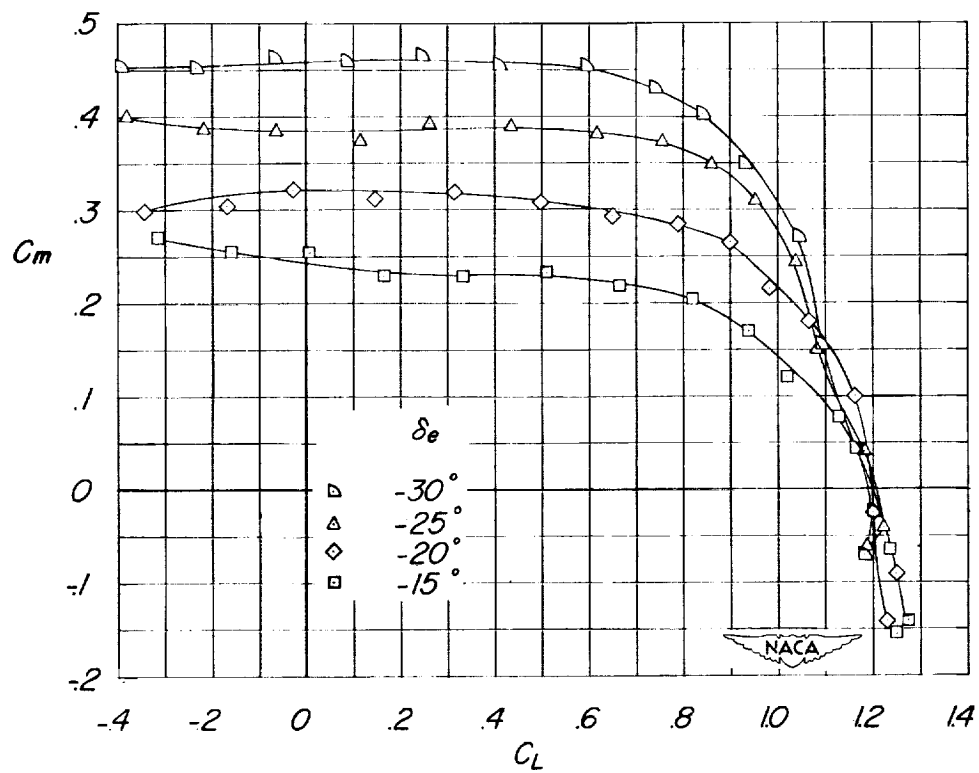
Figure 11.- The effect of elevator deflection on the aerodynamic characteristics of the test model. $i_t = 1^\circ 15'$.



(a) Concluded.

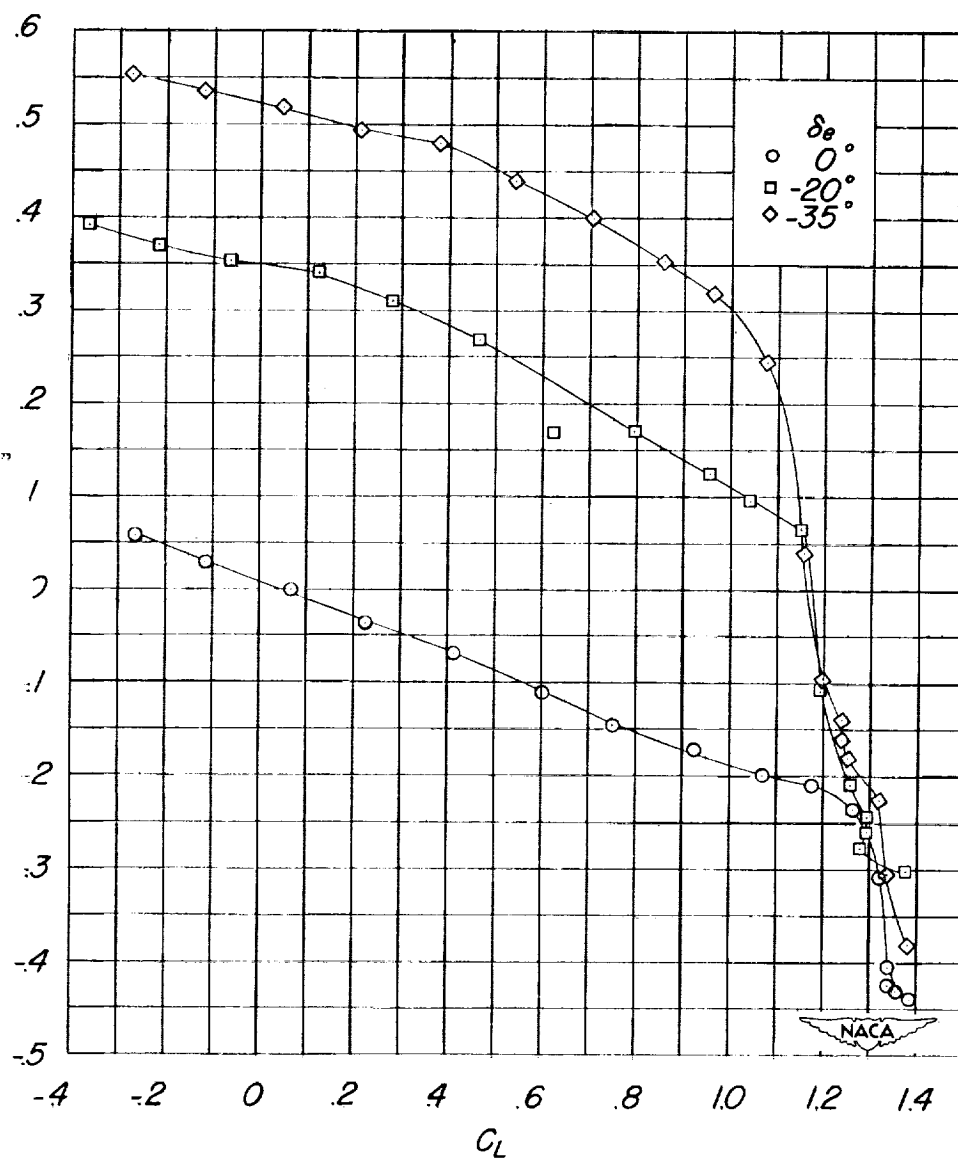
Figure 11.- Continued.

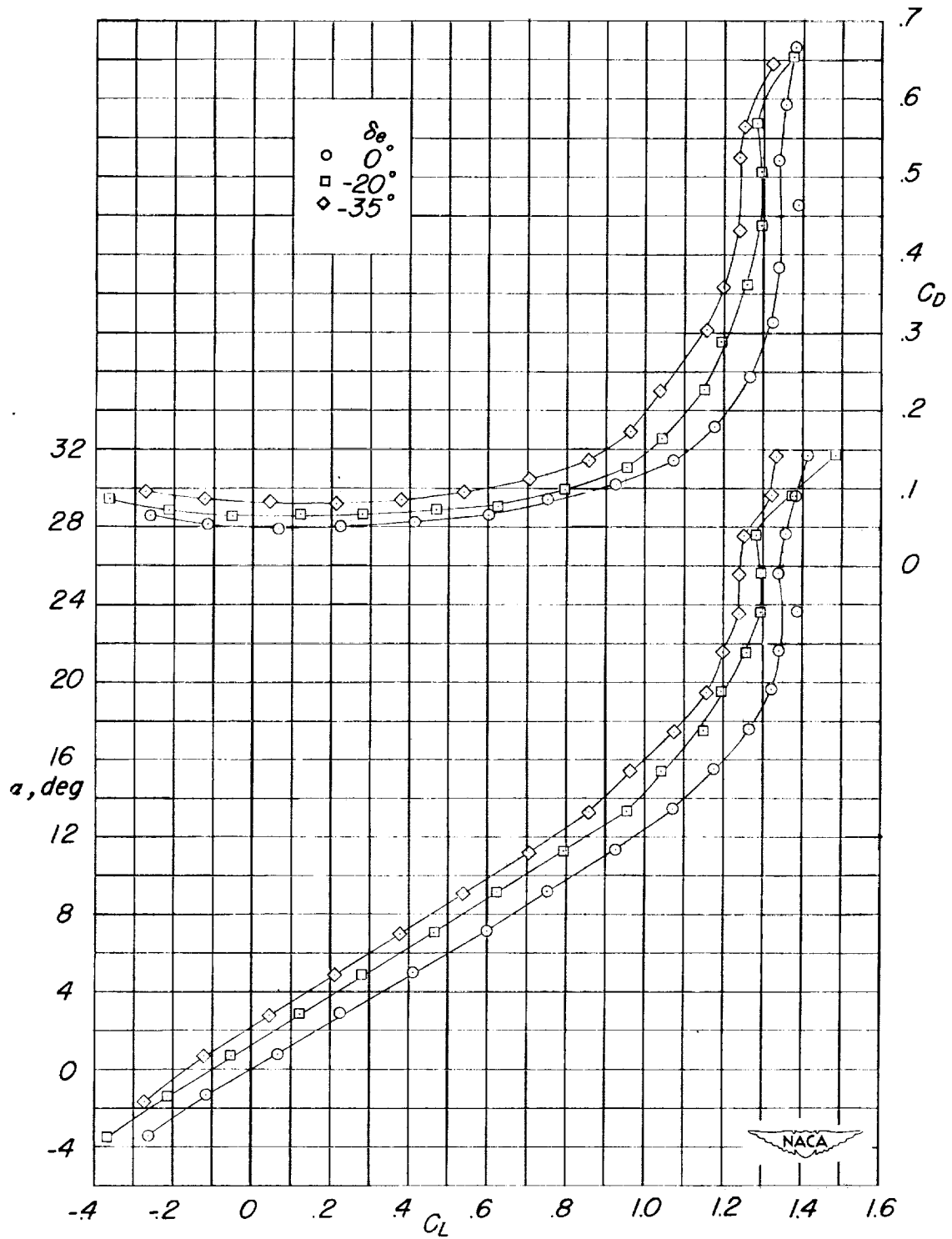
CONCLUDED



(b) Center of gravity at 0.40 M.A.C.

Figure 11.- Continued.





(c) Concluded.

Figure 11.- Concluded.

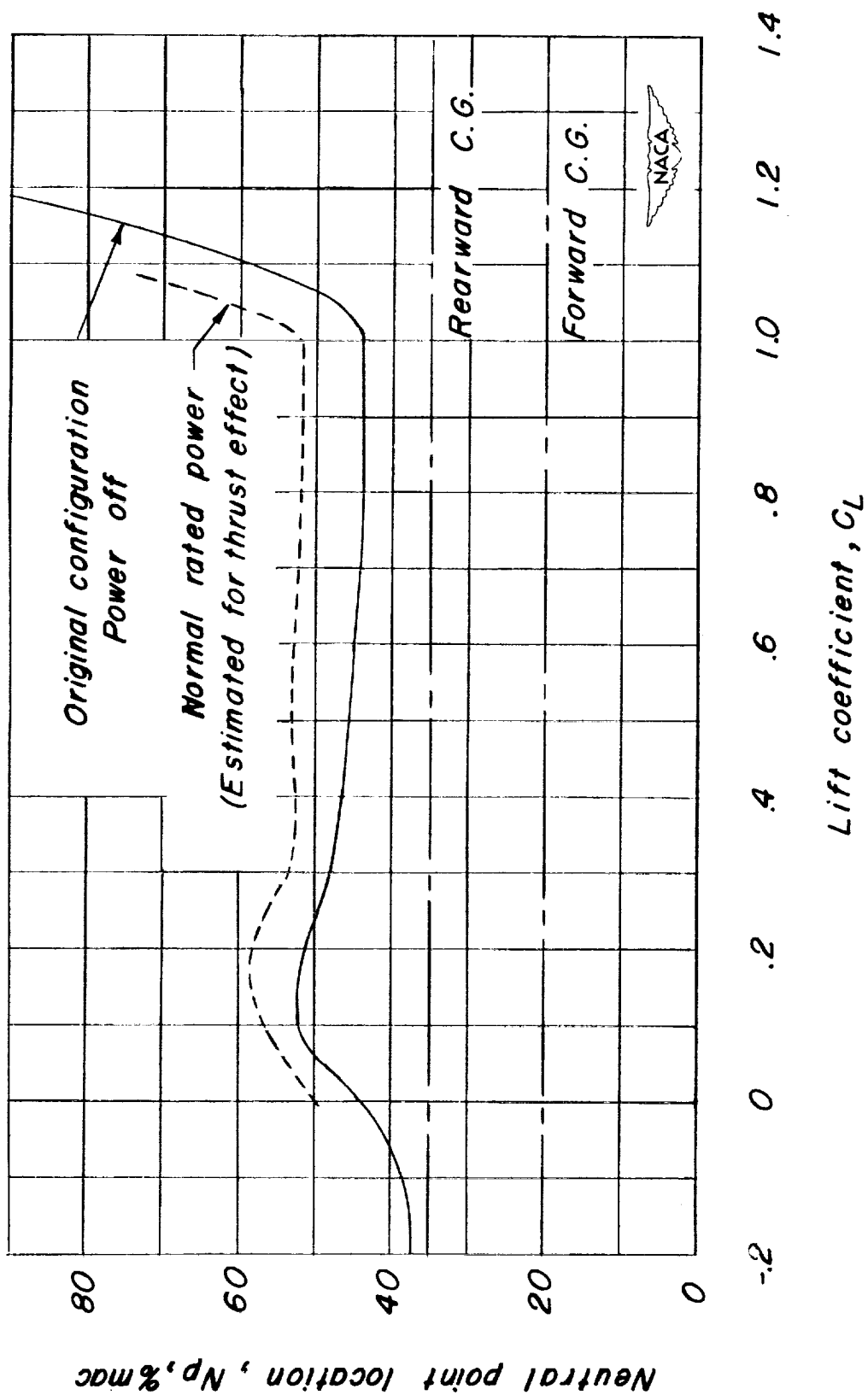


Figure 12.- Elevator-fixed neutral points of the Edo 142 airplane as determined from wind-tunnel test of a $\frac{1}{5}$ -scale model.

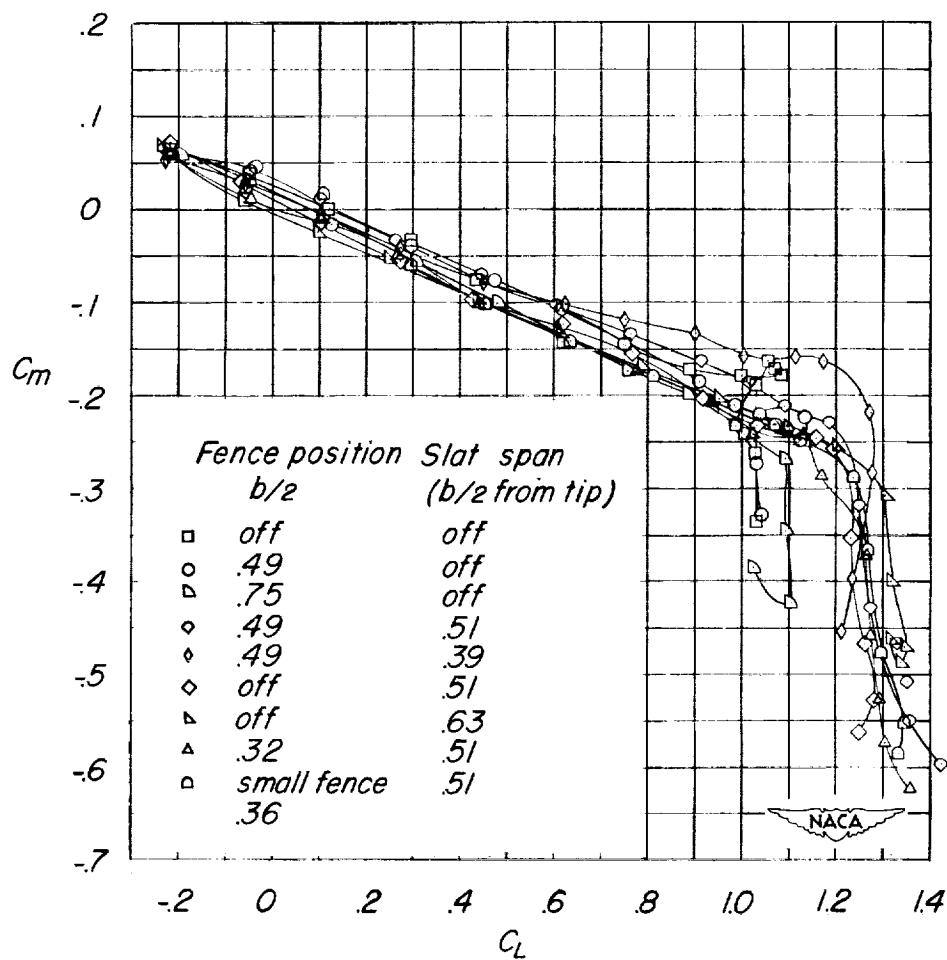


Figure 13.- The effect of stall-control devices on the aerodynamic characteristics of the test model. $i_t = 1^\circ 15'$; center of gravity at 0.25 M.A.C.

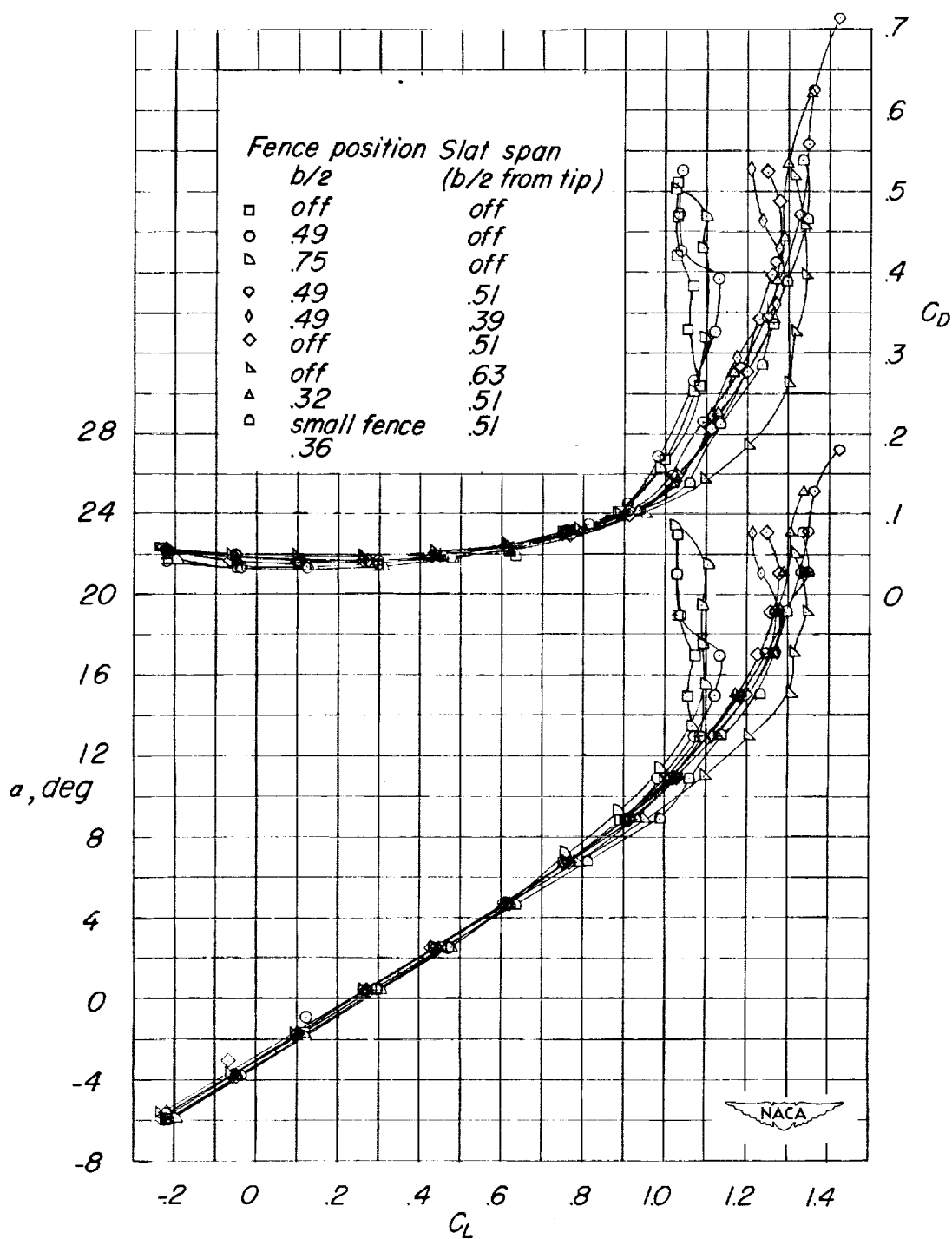


Figure 13.- Concluded.

CONFIDENTIAL

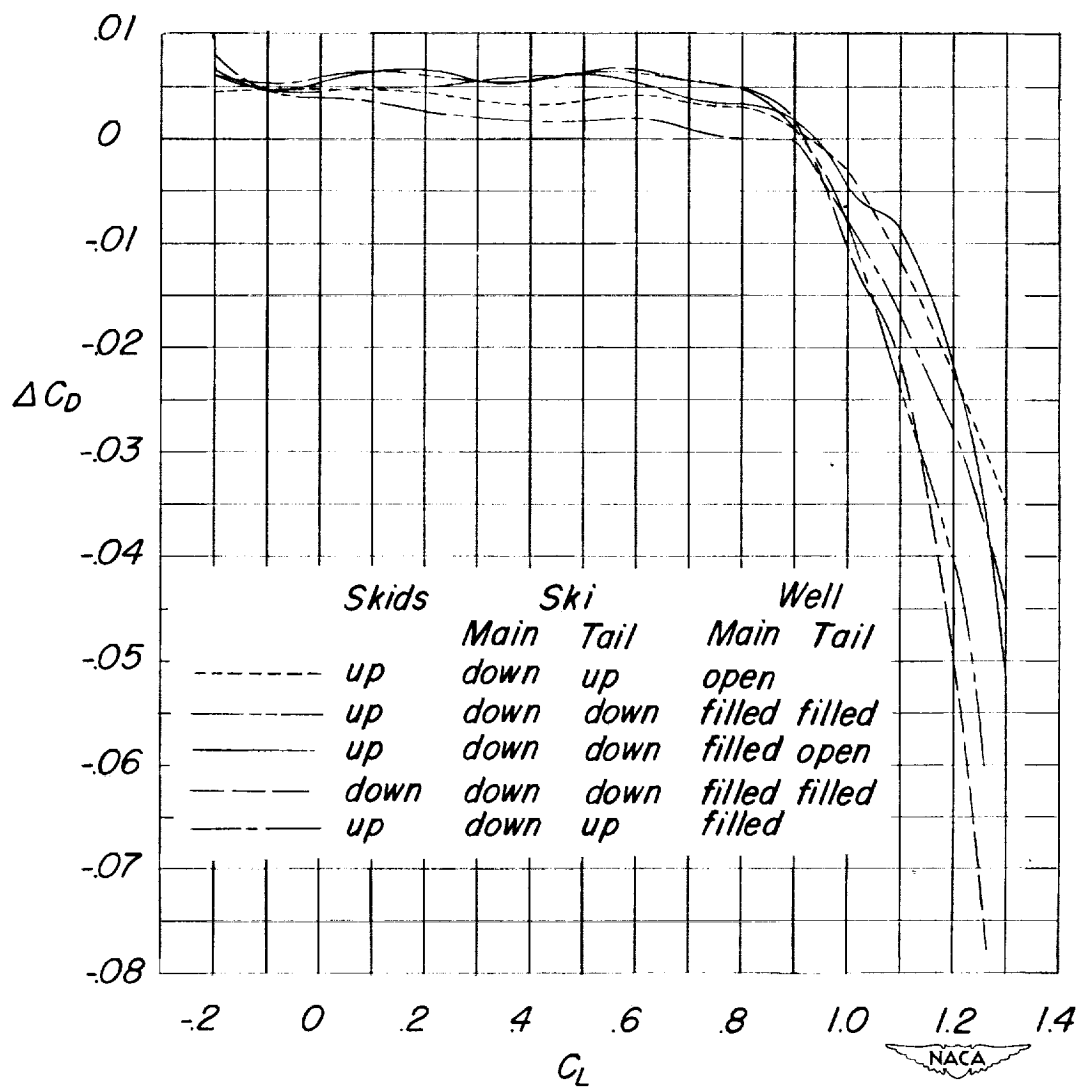


Figure 14.- The effect of the alighting gear on the aerodynamic characteristics of the test model in pitch. $i_t = 1^{\circ}15'$; center of gravity at 0.25 M.A.C.

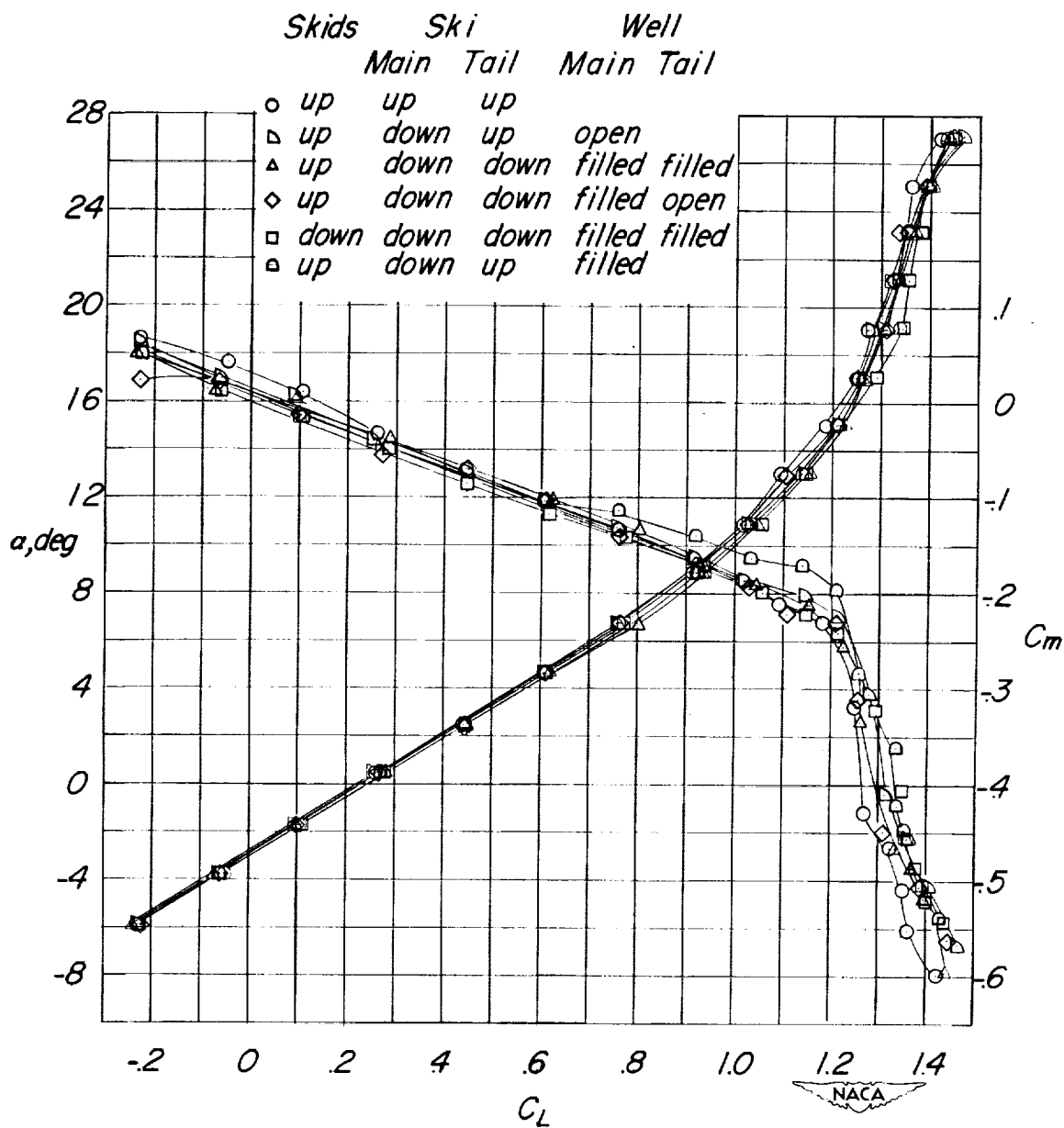
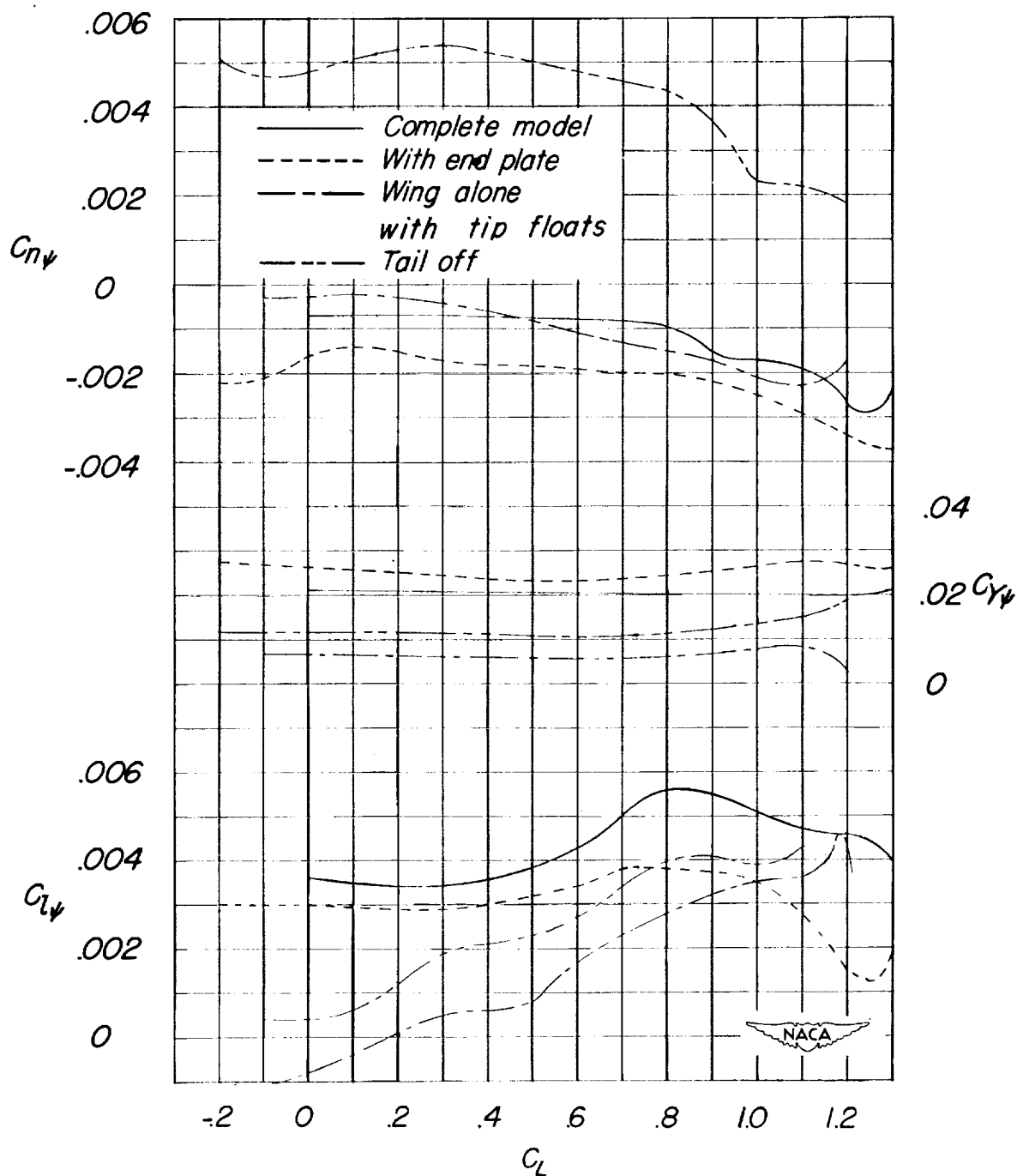
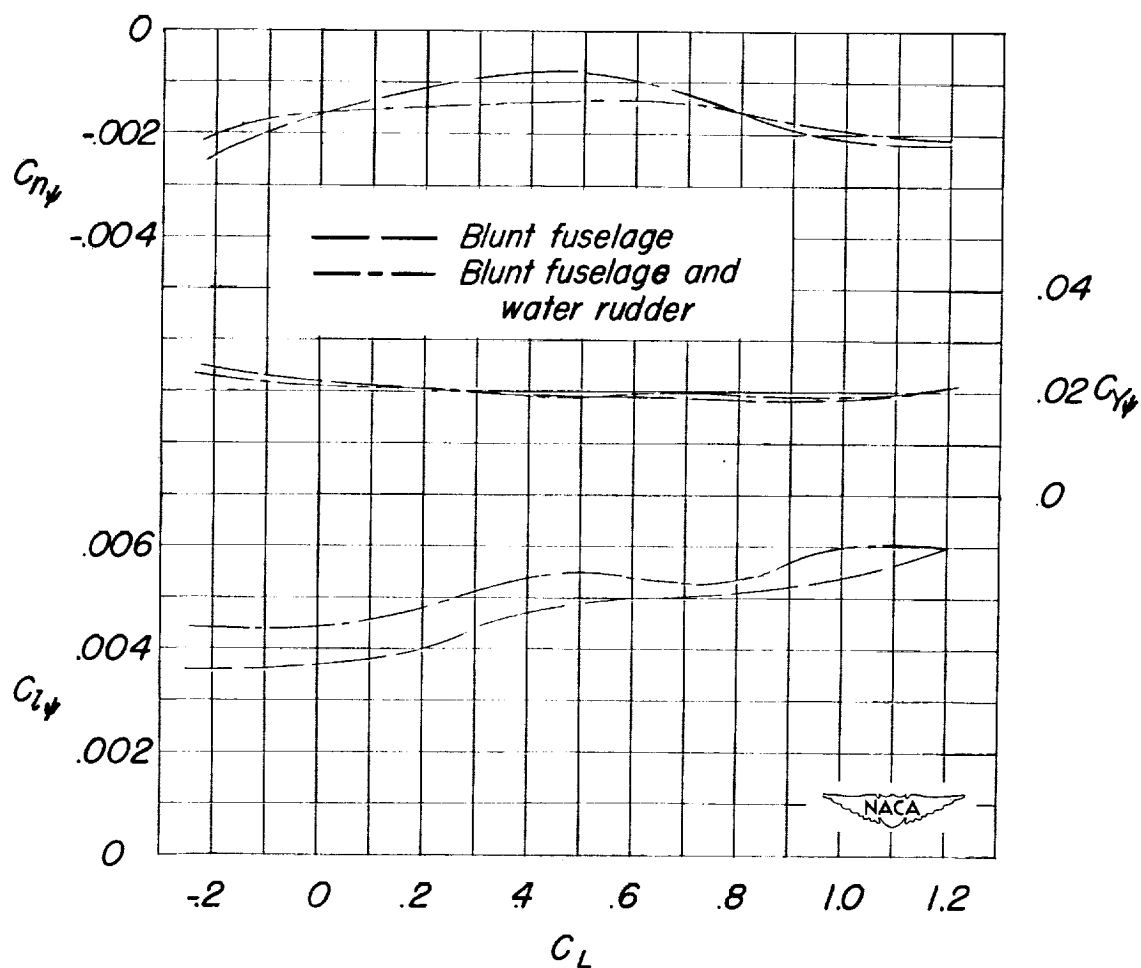


Figure 14.- Concluded.



(a) Original stern configuration.

Figure 15.- The variation of the parameters $C_{n\psi}$, $C_{l\psi}$, and $C_{y\psi}$ with lift coefficient for the test model and constituents. Center of gravity at 0.25 M.A.C.



(b) Revised stern configurations.

Figure 15.- Concluded.

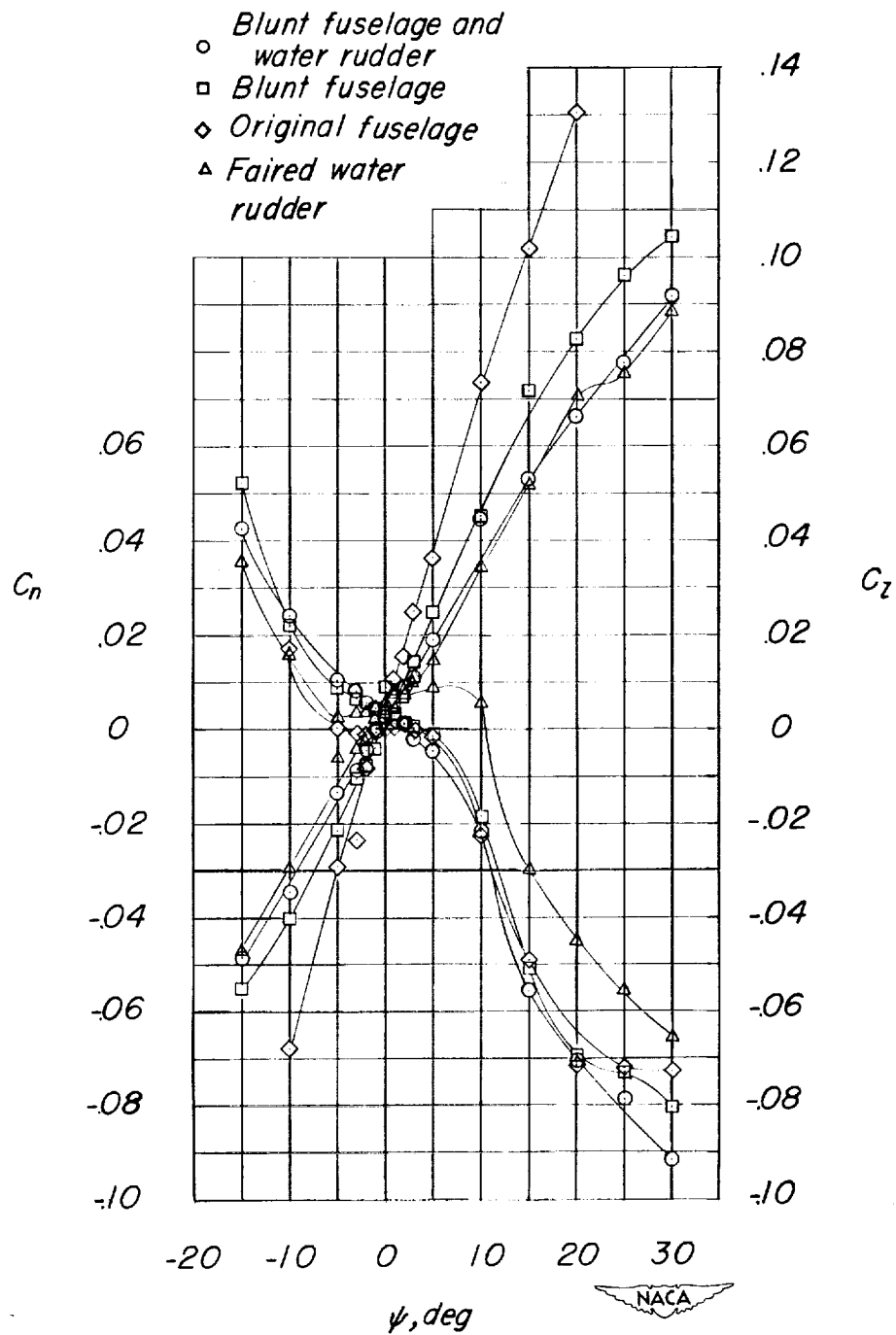
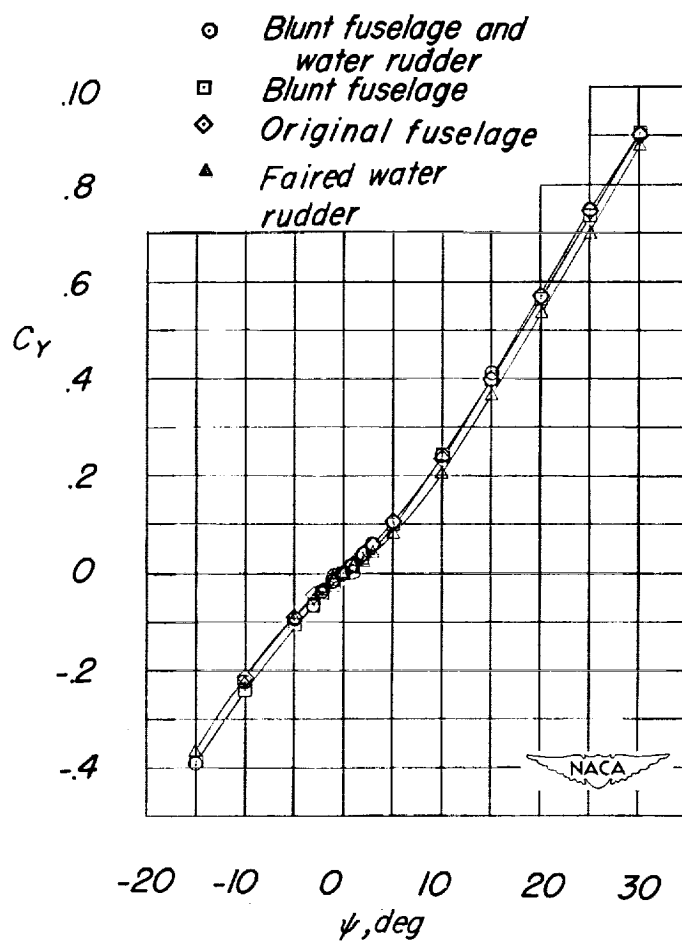
(a) $\alpha = 0^\circ$.

Figure 16.- The aerodynamic characteristics of the test model in yaw.
Center of gravity at 0.25 M.A.C.



(a) Concluded.

Figure 16.- Continued.

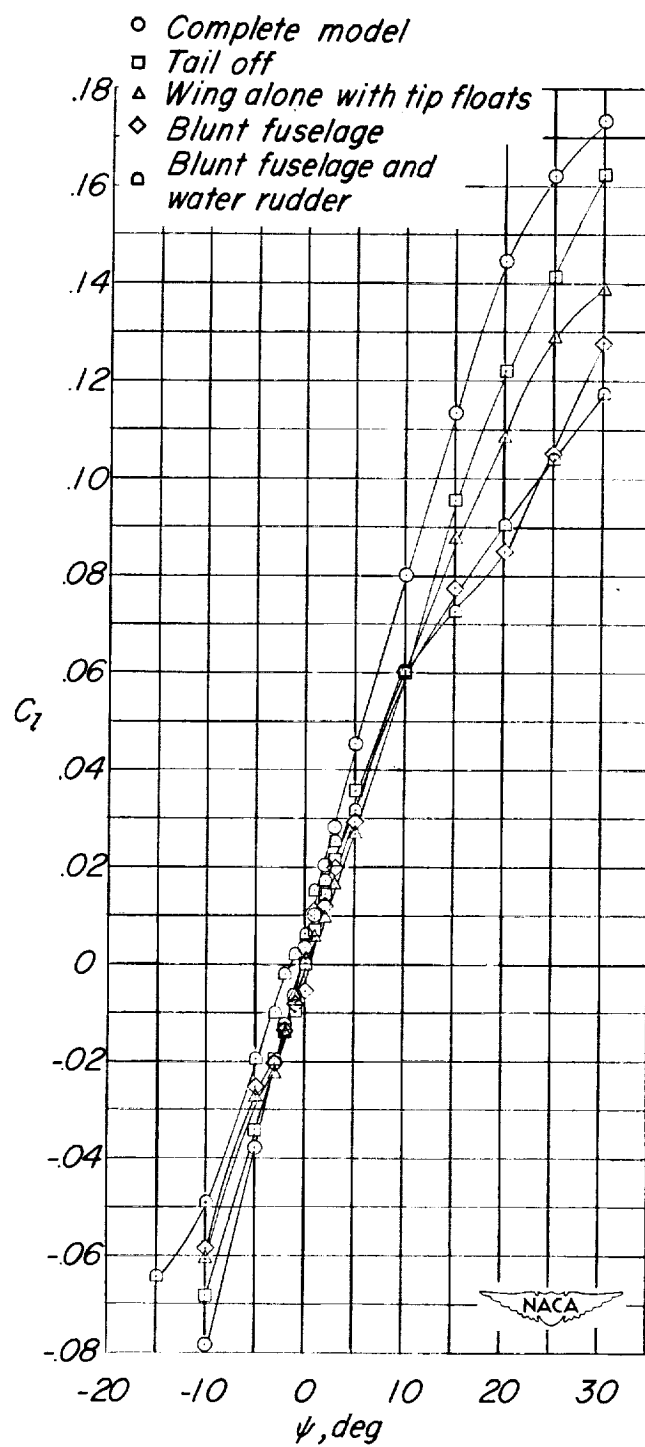
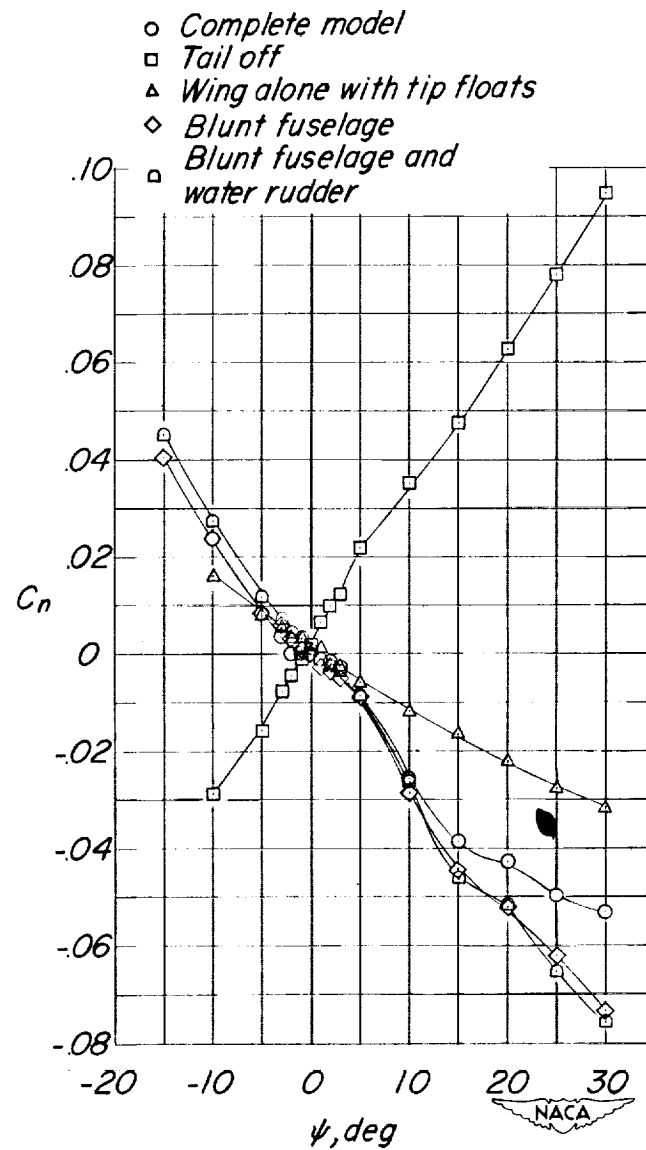
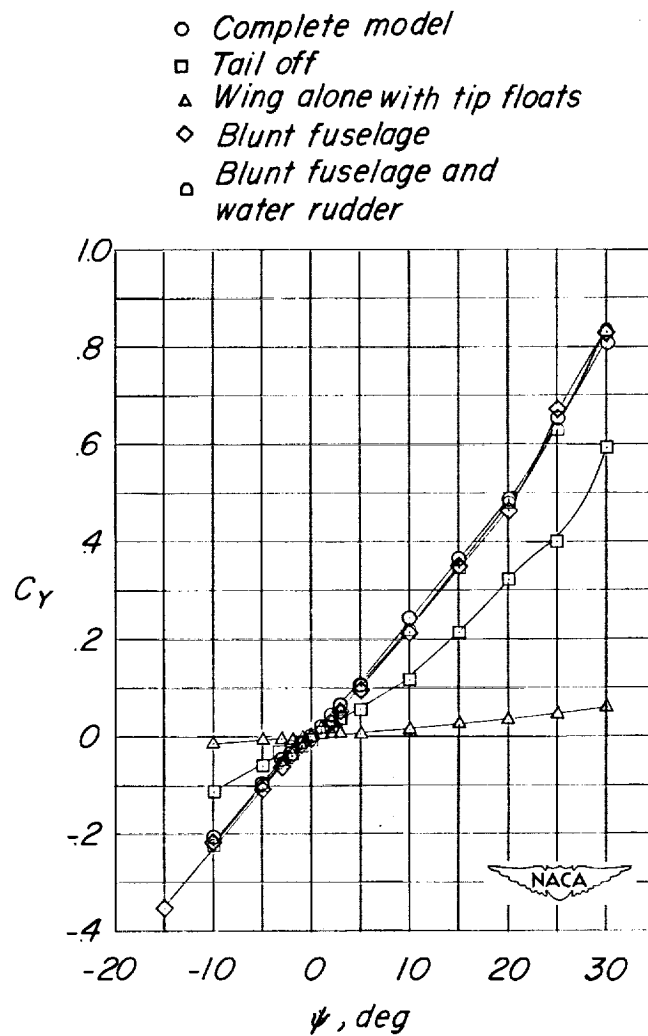
(b) $\alpha = 8^\circ$.

Figure 16.- Continued.



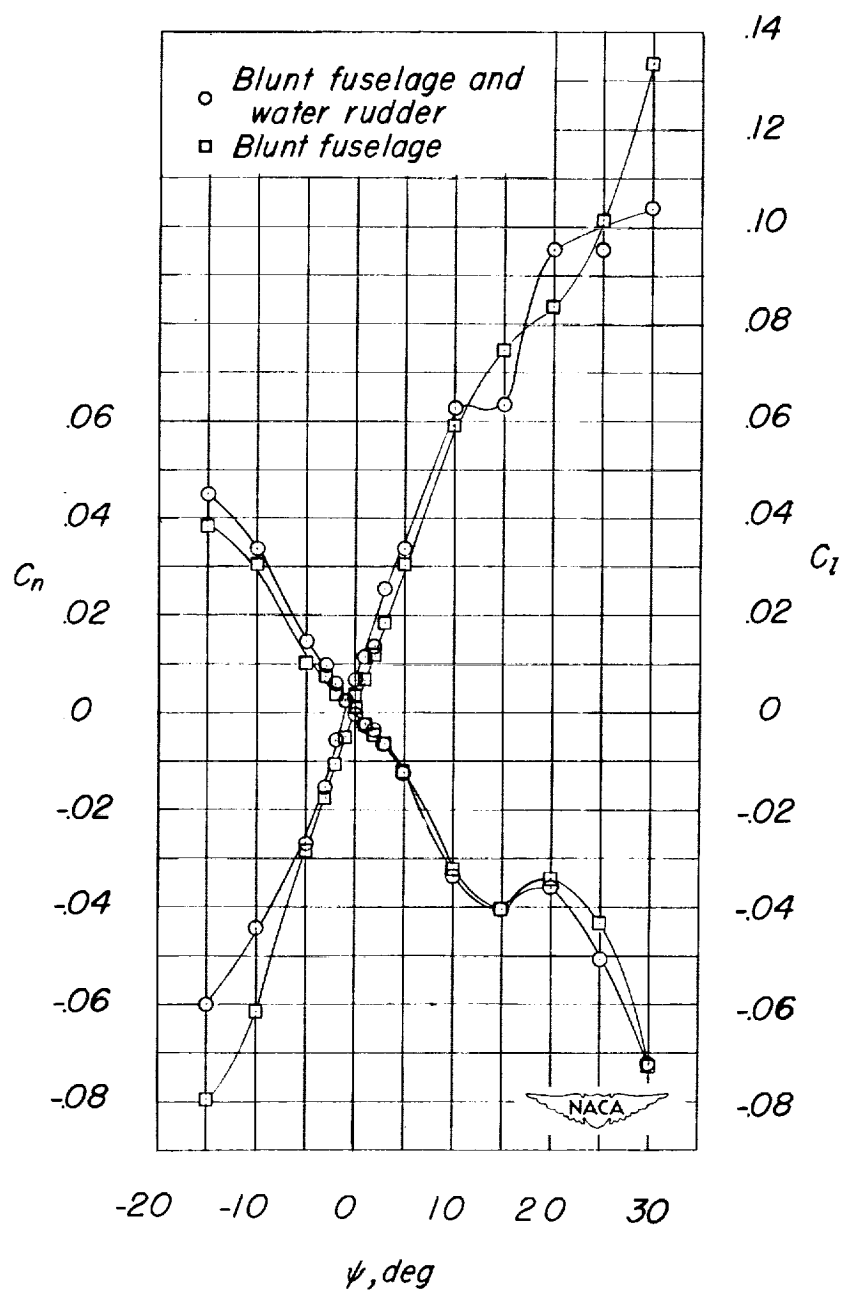
(b) Continued.

Figure 16.- Continued.



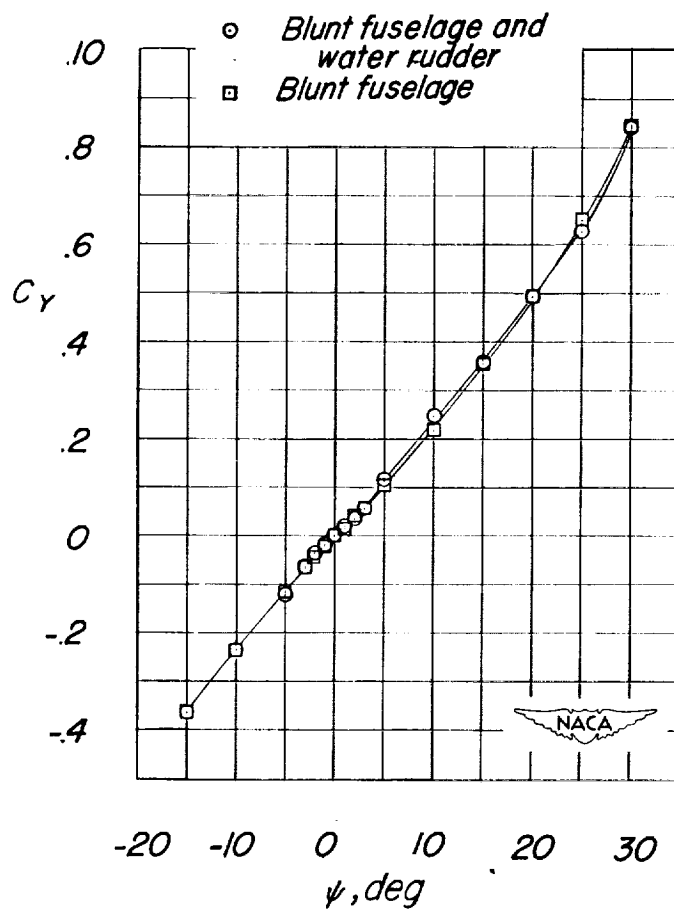
(b) Concluded.

Figure 16.- Continued.



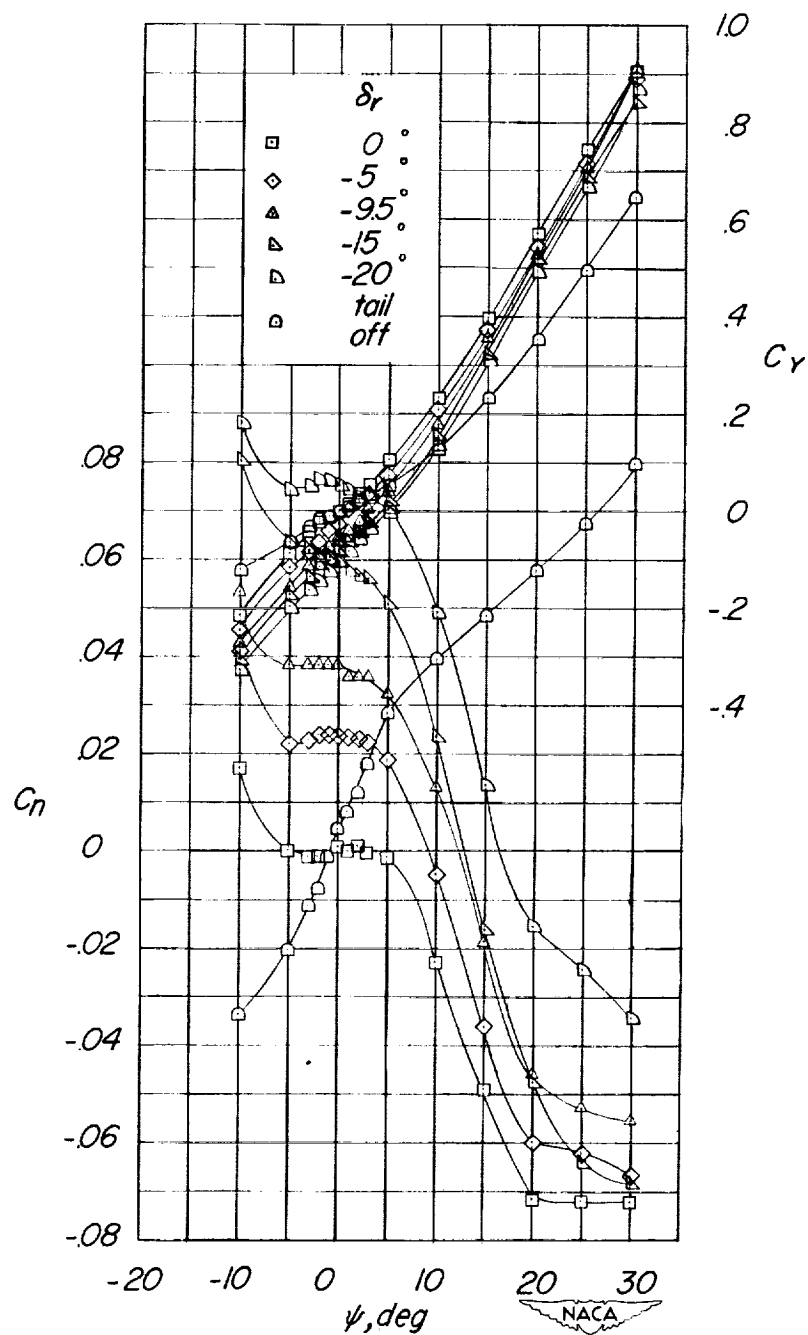
(c) $\alpha = 12^\circ$.

Figure 16.- Continued.



(c) Concluded.

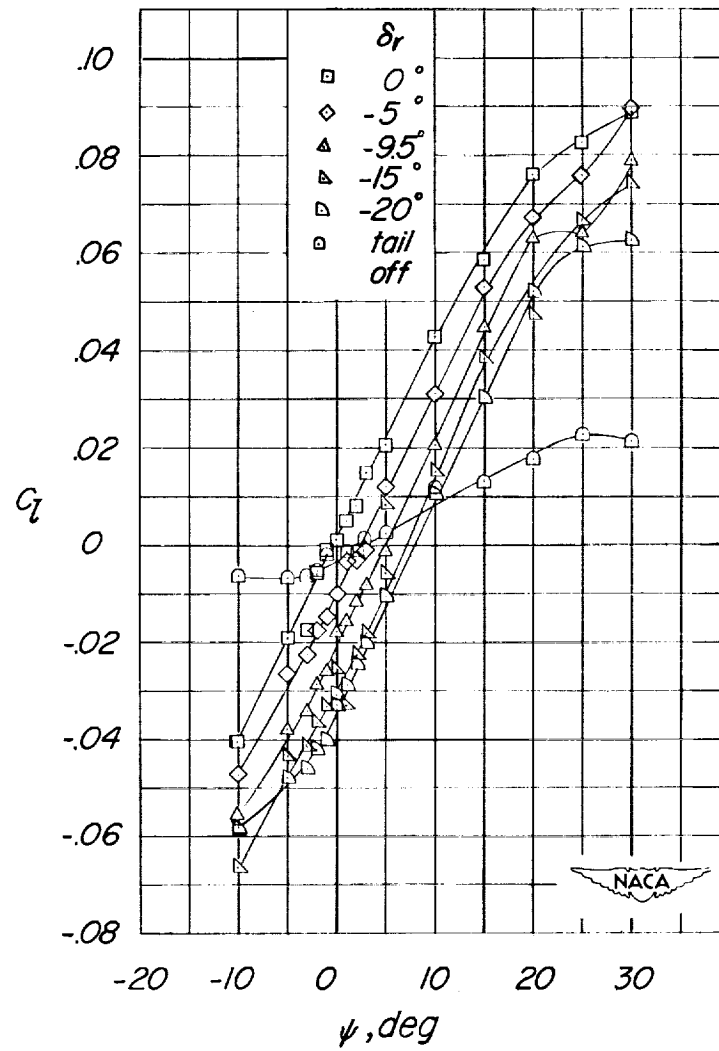
Figure 16.- Concluded.



(a) $\alpha = 0^\circ$; $\delta_{e_{trim}} = 0^\circ$; $i_t = 1^\circ 15'$.

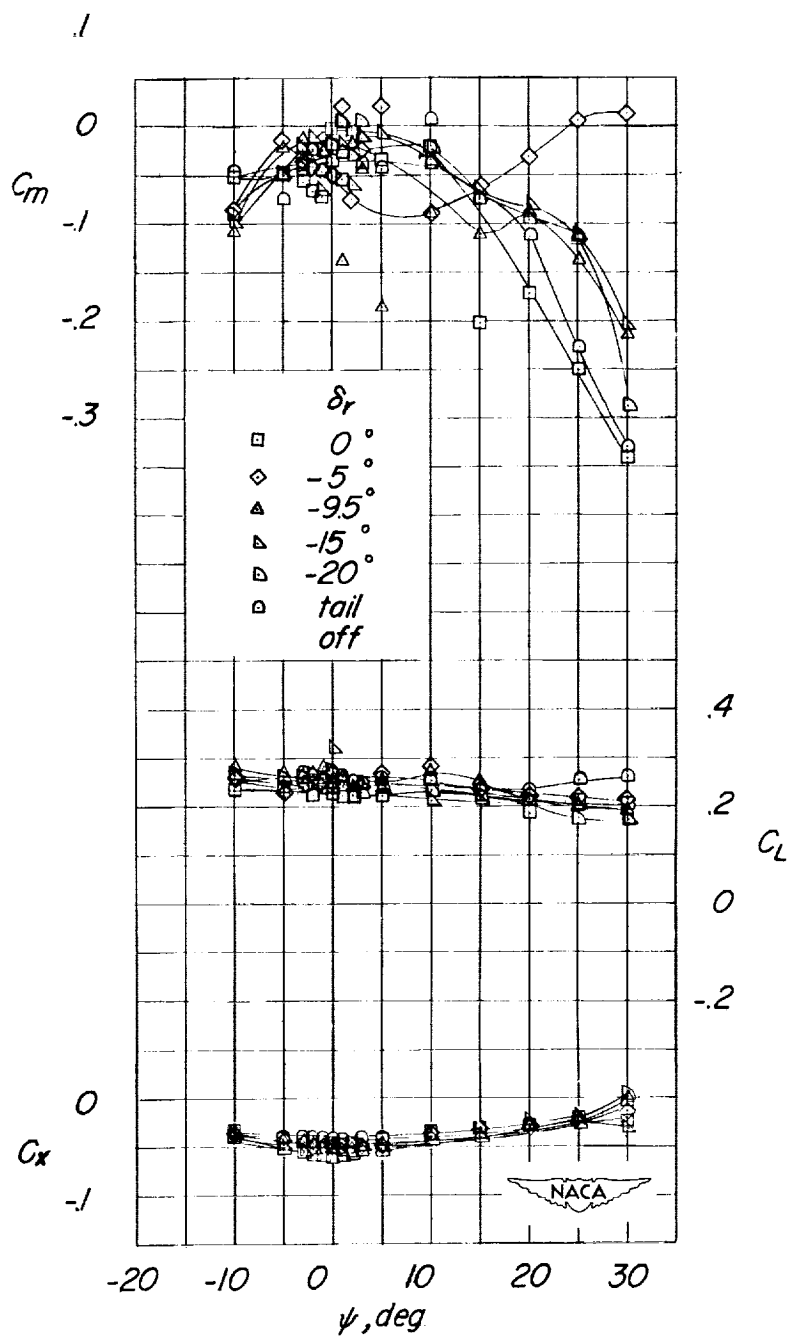
Figure 17.- The effect of rudder deflection on the aerodynamic characteristics of the test model in yaw. Center of gravity at 0.25 M.A.C.

~~CONFIDENTIAL~~



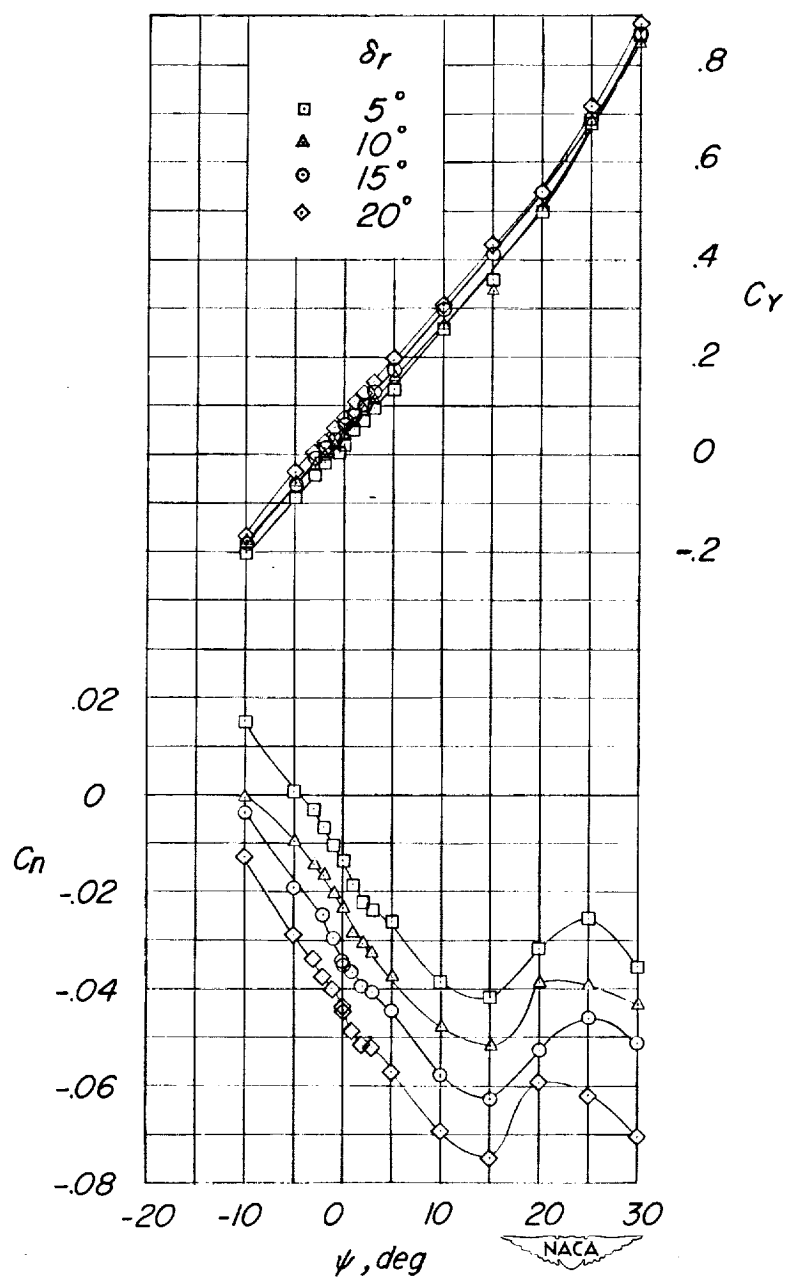
(a) Continued.

Figure 17.- Continued.



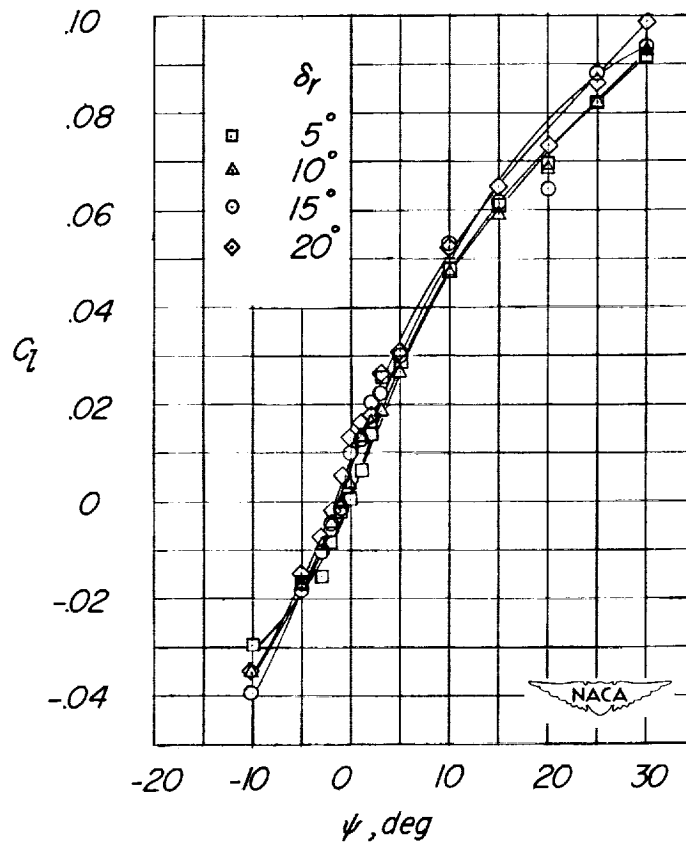
(a) Concluded.

Figure 17.- Continued.



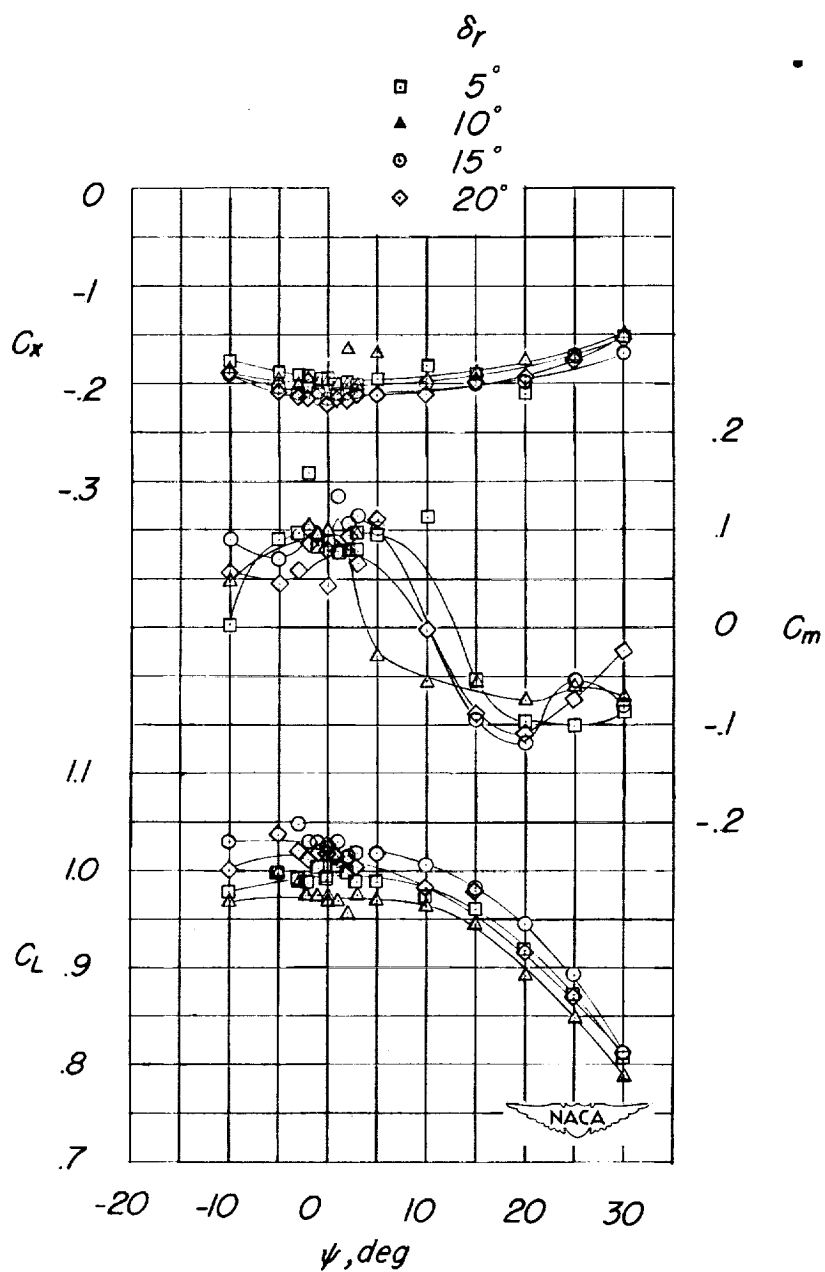
(b) $\alpha = 12^\circ$; $\delta_{e\text{trim}} = -20^\circ$; $i_t = 1^\circ 15'$.

Figure 17.- Continued.



(b) Continued.

Figure 17.- Continued.



(b) Concluded.

Figure 17.- Concluded.

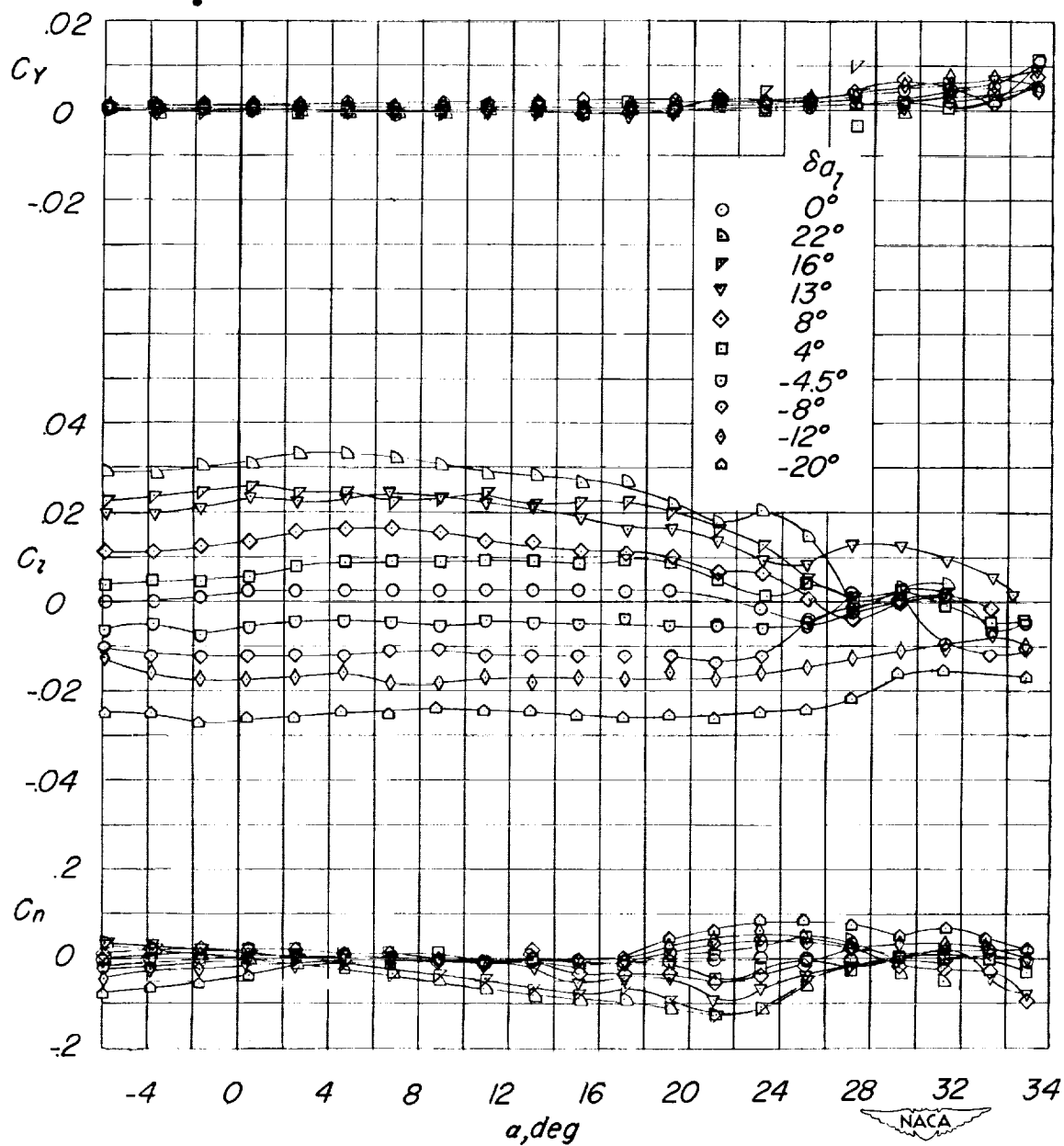


Figure 18.- The effect of left aileron deflection on the aerodynamic characteristics in pitch of the test model.

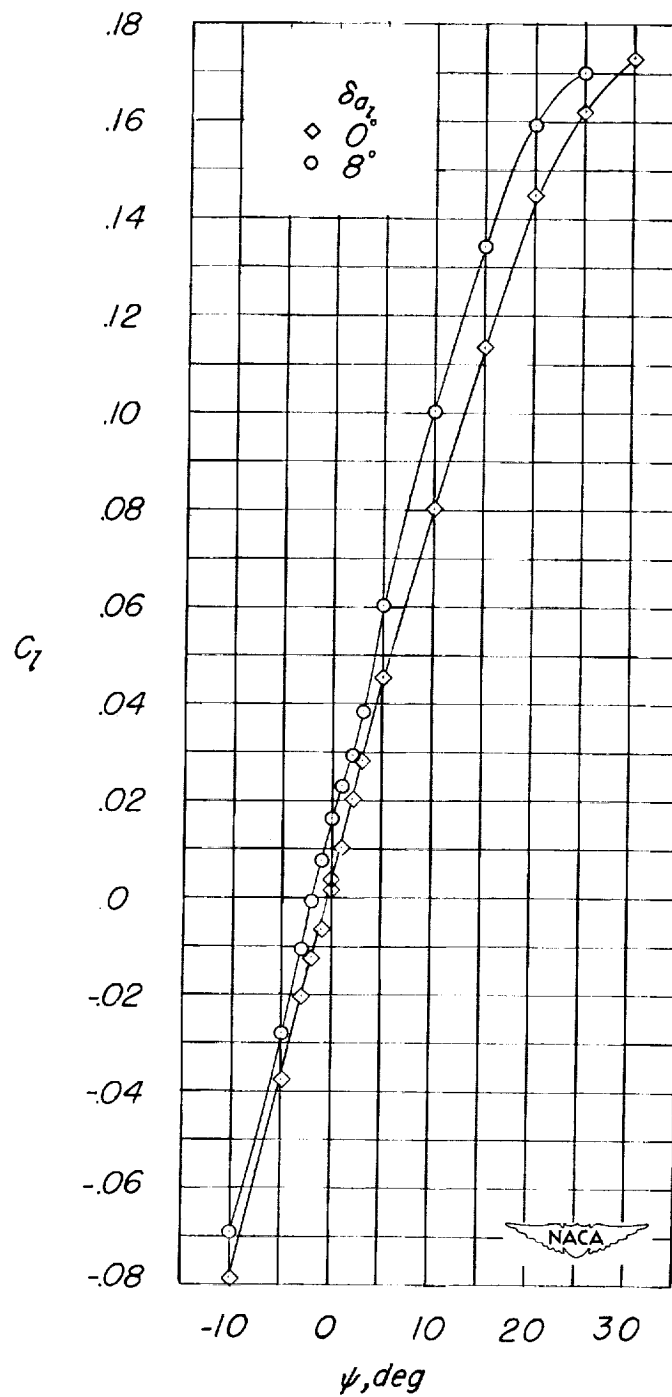


Figure 19.- The effect of left aileron deflection on the aerodynamic characteristics of the test model in yaw. $\alpha = 8^\circ$; $i_t = 1^\circ 15'$.

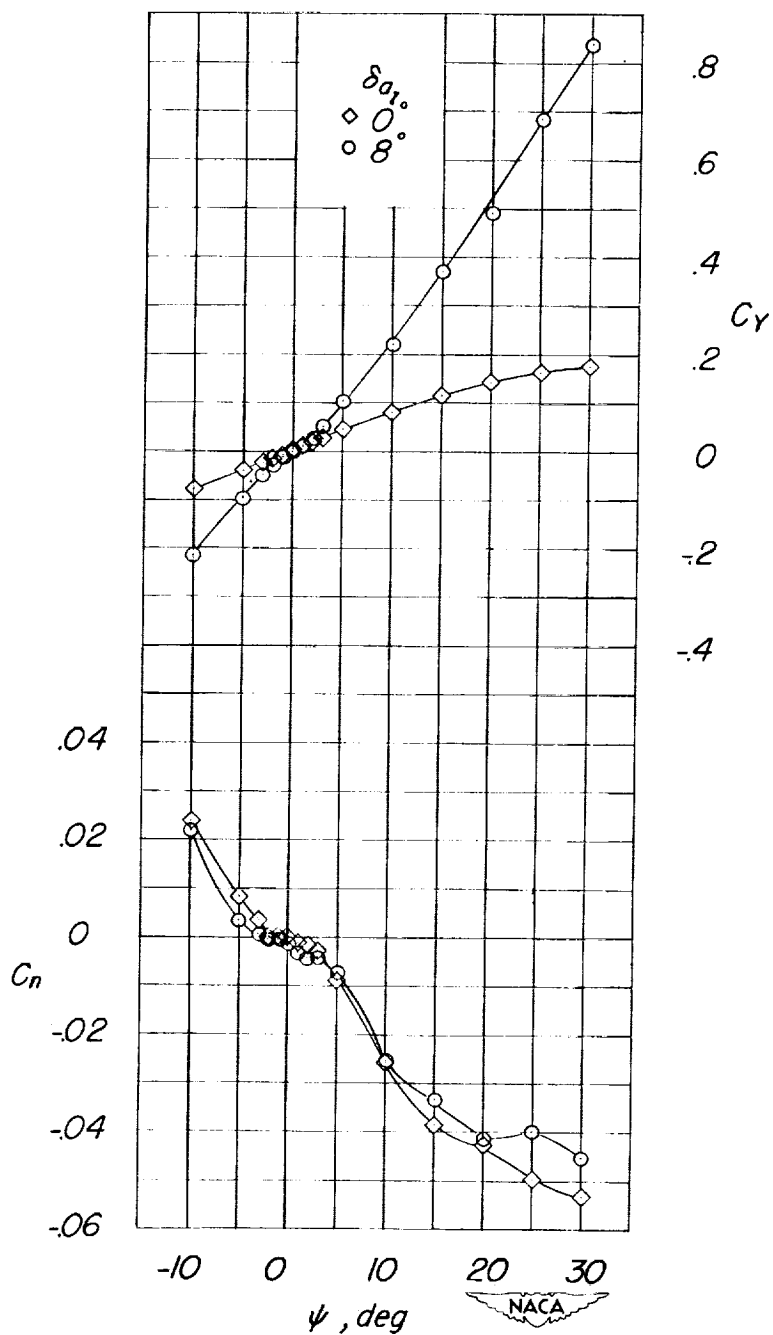


Figure 19.- Concluded.

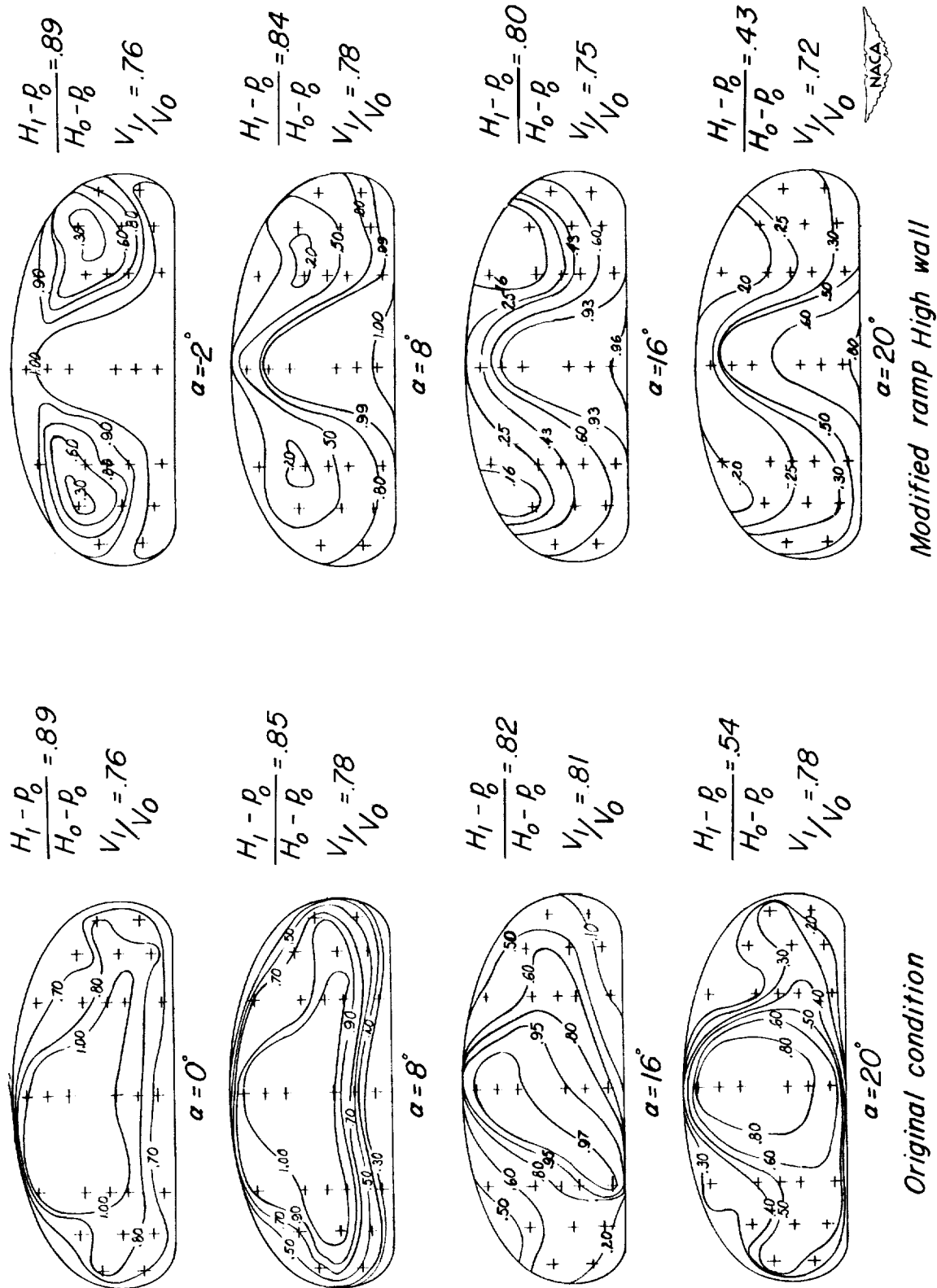


Figure 20.- Ram-recovery-ratio contours at inlet entrance. Station 45.45.

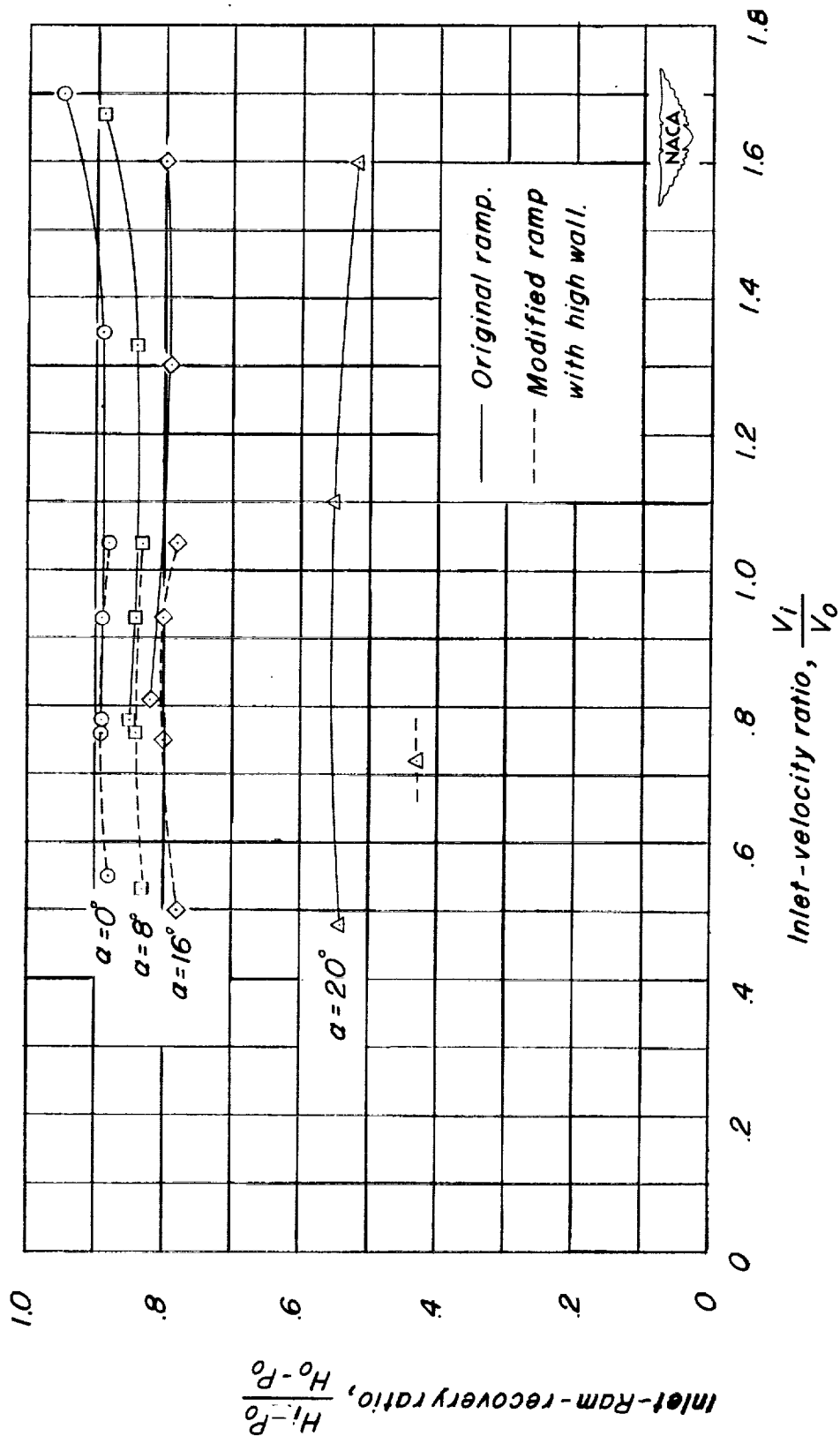


Figure 21.- Variation of inlet-ram-recovery ratio with inlet-velocity ratio for several angles of attack.

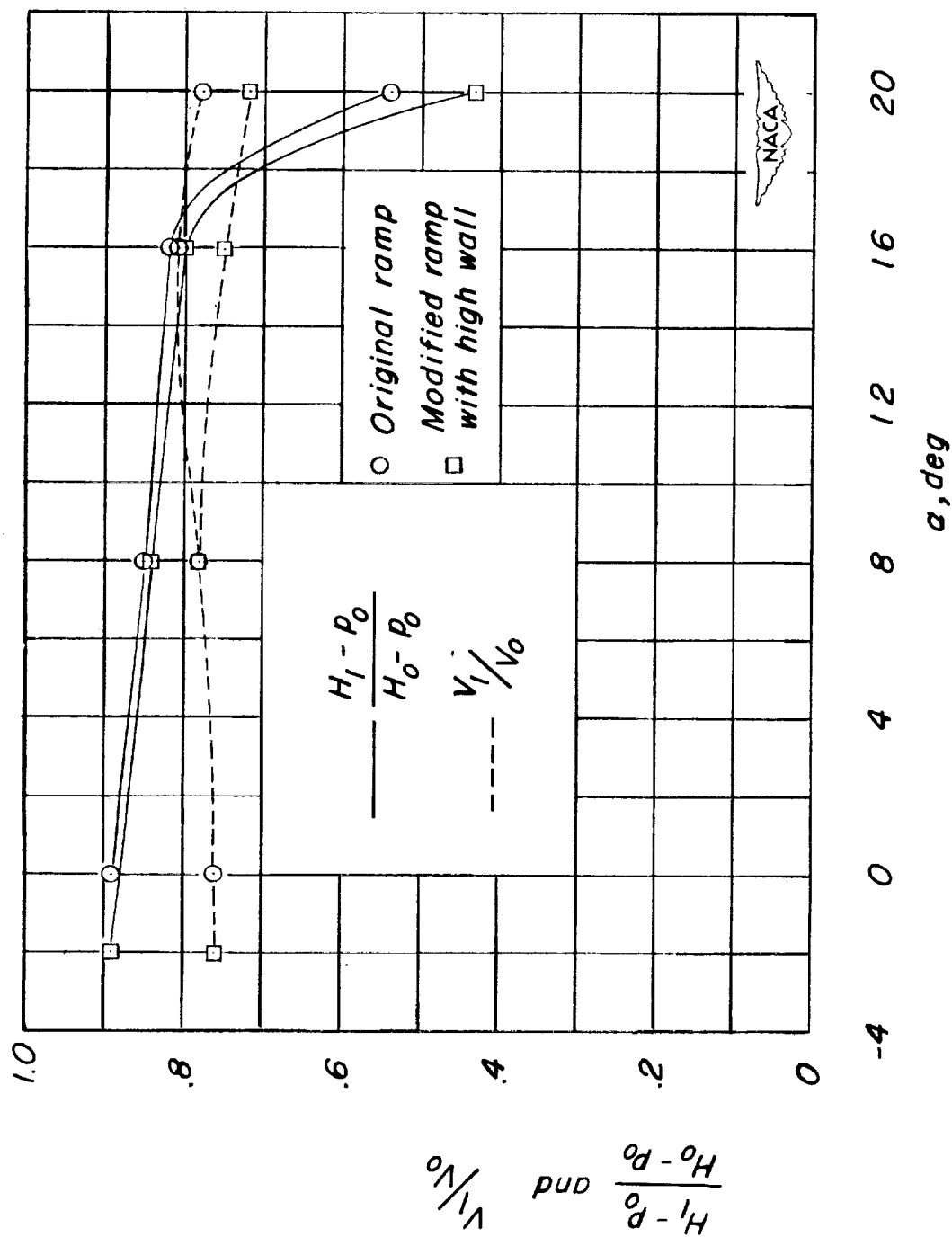


Figure 22.- Effect of angle of attack on the ram-recovery ratio and the velocity ratio at the duct inlet.

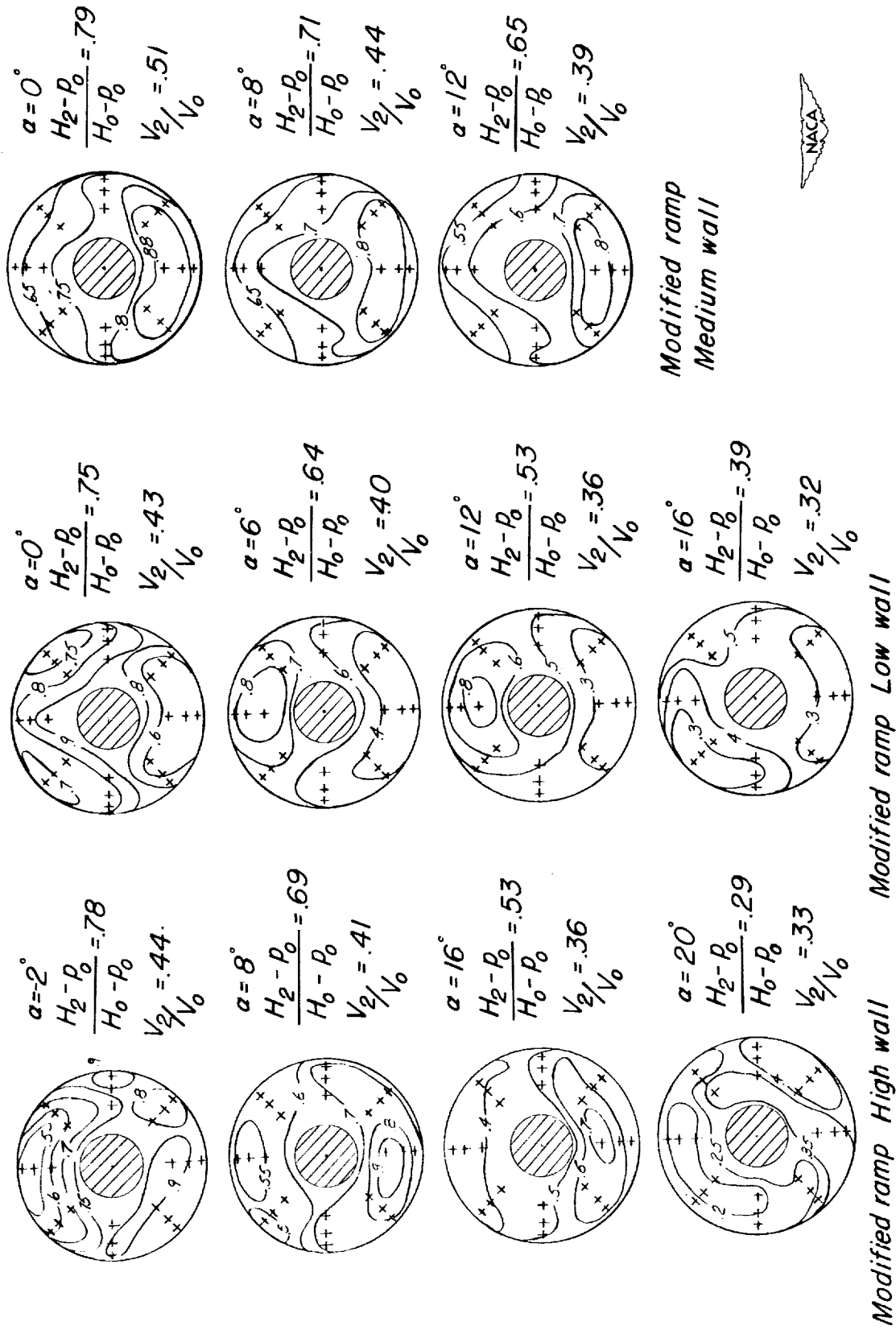


Figure 23.- Ram-recovery-ratio contours at compressor entrance.
Station 53.1.

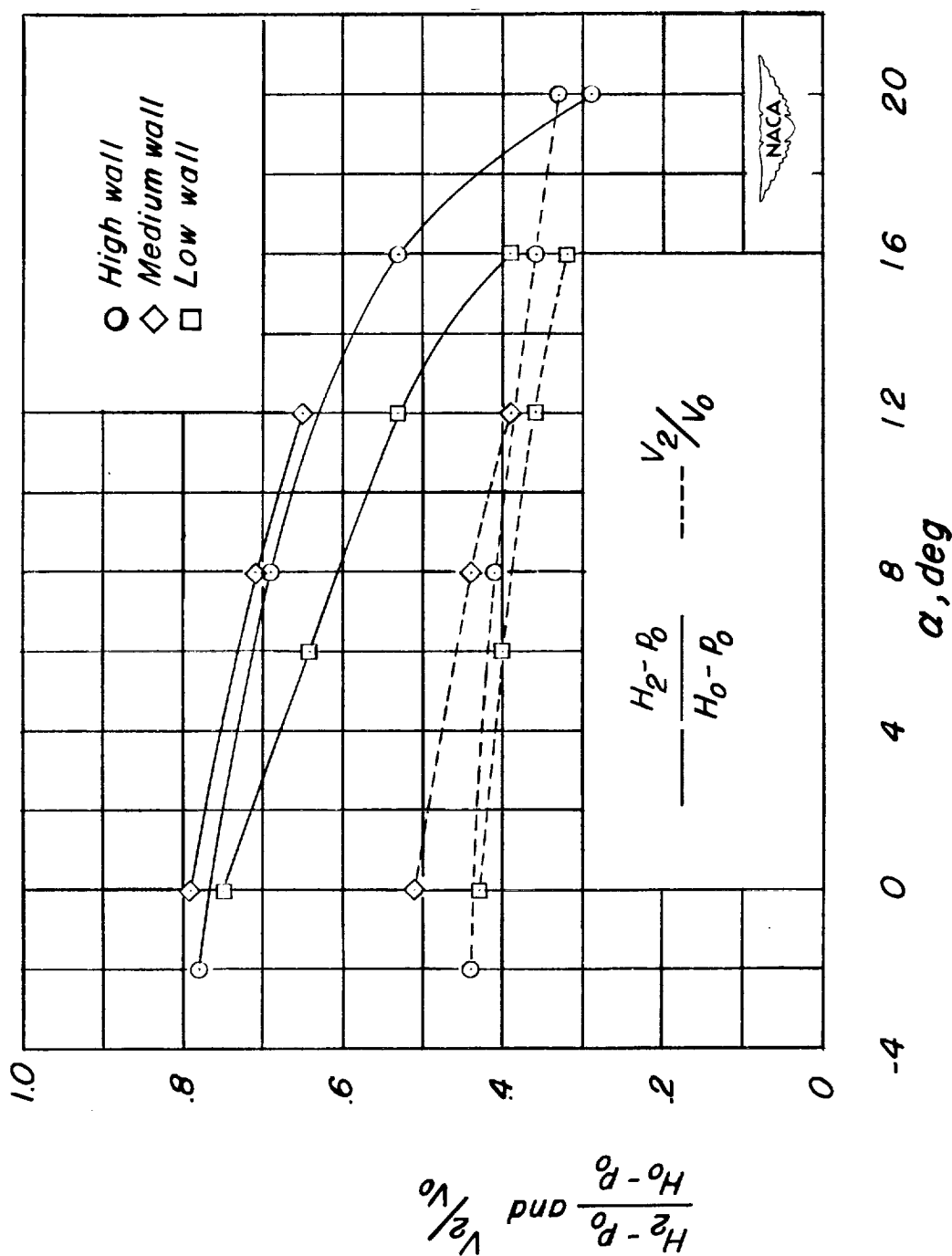


Figure 24.- Effect of angle of attack on the ram-recovery ratio and the velocity ratio at the compressor entrance.

